NUMERICAL INVESTIGATION OF VARIOUS HEAT TRANSFER MECHANISMS ON THERMAL MANAGEMENT OF A LITHIUM-ION BATTERY PACK

A Thesis Submitted to
the Graduate School of Engineering and Sciences of
İzmir Institute of Technology
in Partial Fulfillment of the Requirements for the Degree of

MASTER OF SCIENCE

in Mechanical Engineering

by
Resul Çağtay ŞAHİN

June 2022
İZMİR

ACKNOWLEDGEMENTS

I would like to express my deepest gratitude and sincere thanks to my supervisor Prof. Dr. Erdal ÇETKİN, for bestowing his help and support and paving the way for this study and research.

Secondly, I would like to thank the juries for their attention and comprehensive suggestions for polishing this work.

Besides, I would like to thank all Heat and Mass Transfer Laboratory members. I am genuinely grateful for the experiences that I gathered from Dr. Turgay COŞKUN, İsmail Gürkan DEMİRKIRAN, and Sinan GÖÇMEN.

Finally, yet importantly, I would like to emphasise my sincere gratitude to my family, Öznur, Ekrem, and Şamilhan ŞAHİN, for their precious support. I would like to thank my uncle Ali UTKU for teaching me crucial details about academic writing and thesis defence. Last but not least, I would like to thank Enfal ERKAN, for his suggestions for English writing.

ABSTRACT

NUMERICAL INVESTIGATION OF VARIOUS HEAT TRANSFER MECHANISMS ON THERMAL MANAGEMENT OF A LITHIUM-ION BATTERY PACK

Lithium-ion battery packs are preferred in Electrical and Hybrid Vehicles (EVs and HEVs) due to their efficient and stable energy storage characteristics. Battery Thermal Management Systems (BTMS) have vital importance in EVs and HEVs to keep the batteries in desired temperature range to maximize performance and lifetime. Air cooling is a well-known method with the advantages of being simple and light but main concern for air cooling is effectiveness and pressure drops due to low heat capacity and thermal conductivity of air. This work compared various cooling designs for battery modules based on the surface temperature of batteries and the parasitic power consumption. Modules were built with COMSOL Multiphysics 5.5, and their accuracy was validated by experiments. Each module involves an equal number of batteries whose thermal characteristics were simulated by the electrochemical-thermal battery model, the P3D multiscale model. As a result, the maximum temperature was reduced by 5% (1.8°C) for inline alignment with baffles and 7.2% (2.8°C) for staggered modules, and the temperature gradient was reduced by 40% (1.7°C) for inline and 35% (1.5°C) for staggered alignments. While fan power consumption of inline alignment with triangle baffles (0.98W) was 3.5 times higher than the base design (0.27W), it was 0.23W for staggered design. Moreover, the cooling performance of different winglet parameters was compared and documented.

Keywords: *Battery Thermal Management Systems; P3D Model; Temperature Uniformity; Forced Air Convection; Cylindrical Lithium-ion Battery; Cooling Optimization; Winglets; Baffles; Cooling Efficiency*

ÖZET

ÇEŞİTLİ ISI GEÇİŞİ MEKANİZMALARININ BİR LİTYUM-İYON BATARYA PAKETİNİN ISIL YÖNETİMİ İÇİN SAYISAL OLARAK İNCELENMESİ

Diğer alternatiflerinden daha verimli ve sağlıklı çalıştıkları için Lityum-iyon bataryalar, günümüz elektrikli araçlarında en çok tercih edilen batarya türüdür. Ancak, Lityum-iyon bataryaların ömrü ve verimliği çalışma koşullarına bağımlıdır. Çalışma sıcaklığı batarya sağlığını etkilediği ve ölümcül kazalara yol açabileceği için dikkatle kontrol edilmelidir. Bu etkileri en aza indirmek, güvenli ve stabil bir kullanım sağlamak için batarya termal yönetim sistemleri (BTYS) elektrikli araçlar için hayati öneme sahiptir. Halihazırda kullanılan birçok verimli metot olmasına rağmen, hava soğutmalı batarya paketleri gerek hafif ve basit tasarım özellikleri gerekse ucuz üretim ve bakım maliyetleri bakımından halen elektrikli araç üreticileri tarafından tercih edilmektedir. Havanın termofiziksel özellikleri nedeniyle hava soğutmalı batarya paketlerinin performansı sıvı soğutma metotlarına nazaran düşük kalmaktadır. Bu nedenle hava soğutmalı sistemlerin iyileştirilmesi gerekmektedir. Bu tez, silindirik bataryalardan oluşan hava soğutmalı bir batarya modülünün performansını, bataryaların fazla ısındığı bölgelerdeki akışı çeşitli akış karıştırıcılarla değiştirerek ısı transferini arttırmayı ve homojen bir batarya sıcaklık dağılımı sağlamayı amaçlamaktadır. Tasarım iyileştirmeleri, COMSOL Multiphysics 5.5 yazılımı ile türbülanslı akış ve P3D olarak da bilinen batarya termal modelini birleştirerek oluşturulan simülasyonlar yardımı ile yapılmıştır. Ayrıca, simülasyonların tutarlılığı deneysel verilerle karşılaştırılarak doğrulanmıştır. Sonuç olarak, hizalanmış yerleşimdeki batarya modülünde maksimum sıcaklıklar %5 (1.8ºC) ve sıcaklık dağılımı 40% (1.7ºC) akış karıştırıcılar yardımı ile iyileştirilmiştir. Ayrıca, çapraz konumlandırılmış bataryalar maksimum sıcaklığı ve sıcaklık dağılımını sırasıyla, %7.2 (2.8ºC) ve %35 (2.5ºC) iyileştirmiştir. Son olarak, bu iyileştirmeler yeni tasarım için yaklaşık 0.7W'lık bir güç tüketimi artışı ile sağlanmıştır.

Anahtar Kelimeler: *Batarya Termal Yönetim Sistemleri; P3D Batarya Modeli; Homojen Sıcaklık Dağılımı; Silindirik Lityum-iyon Bataryalar; Soğutma İyileştirmeleri; Girdap Oluşturucu; Akış Karıştırıcı; Soğutma Verimi; Zorlanmış Hava Taşınımı.*

TABLE OF CONTENTS

LIST OF FIGURES

Figure **Page**

Figure **Page**

LIST OF TABLES

Table **Page**

LIST OF SYMBOLS

A	polynomial coefficients
a_s	effective surface area [m^{-1}]
c	lithium concentration [mol m^{-3}]
C_μ	turbulence model constant
$C_{\varepsilon 1}$	turbulence model constant
$C_{\varepsilon 2}$	turbulence model constant
Cp	specific heat capacity [J kg^{-1} K^{-1}]
D	diffusion coefficient [m^2 s^{-1}]
E_{eq}	equivalent potential [V]
f	fanning friction factor
$f_\pm$	molar salt activity coefficient
F	Faraday constant [C mol^{-1}]
h	convective heat transfer coefficient [W m^{-2} K^{-1}]
i_0	reference exchange current density [A m-2]
i	current density [A m^{-2}]
I_{app}	applied current to battery [A m^{-2}]
j^{Li+}	reaction current density [A m^{-2}]
k	thermal conductivity [W m^{-1} K^{-1}] or turbulent kinetic energy [m^2s^{-2}]
l_T	turbulent length scale [m]
L_T	characteristic length [m]
L	length [µm]
n	normal vector

N_{batt} number of batteries

Nu Nusselt number

p_0 outlet pressure [Pa]

P_k production number

P_{fan} fan power consumption [W]

P_{Vol} volumetric power efficiency [Wl^{-1}]

P pressure [Pa]

Q heat generation rate [$W\ m^{-3}$]

r radius [m]

r_p particle radius [µm]

R universal gas constant [$J\ mol^{-1}\ K^{-1}$]

SoC state of charge

S_x battery distance in flow direction [mm]

S_y battery distance in transverse direction [mm]

t_+^0 transference number

T temperature [°C]

U_{in} inlet velocity [m/s]

x coordinate & cathode SoC

y anode state of charge

Greek Letters

α transfer coefficient

β Bruggemann tortuosity coefficient

ΔT temperature difference [°C]

ε volume fraction rate and turbulence dissipation rate [m^2s^{-3}]

η overpotential [V] / heat transfer performance coefficient

κ ionic conductivity [S m^{-1}]

μ kinematic viscosity [m^2s^{-1}]

ρ density [kg m^{-3}]

σ electronic conductivity [S m^{-1}]

σ_k turbulent flow constant

σ_ε turbulent flow constant

Φ potential [V]

Subscripts and Superscripts

amb ambient conditions

$batt$ battery

b baffled design

eff effective

in inlet

irr irreversible

l liquid state

neg negative electrode

ohm ohmic

out outlet

pos positive electrode

rev reversible

s solid state

sep	separator
$tang$	tangential
tot	total
T	turbulence

LIST OF ABBREVIATIONS

DFIC	Dielectric Fluid Immersion Cooling
EC	Ethylene Carbonate
EMC	Ethyl Methyl Carbonate
EV	Electric Vehicle
HEV	Hybrid Electric Vehicle
IC	Initial Conditions
LCO	Lithium Cobalt Oxide Battery
LFP	Lithium Iron Phosphate Battery
LIB	Lithium-ion Battery
LMO	Lithium Manganese Oxide Battery
LNO	Lithium Nickel Oxide Battery
NCA	Lithium Nickel Cobalt Aluminum Oxide Battery
NMC	Lithium Nickel Manganese Cobalt Oxide Battery
P3D	Pseudo-3D
PCM	Phase Change Material
SEI	Solid-Electrolyte Interphase

CHAPTER 1

INTRODUCTION

Nowadays, environmental issues are undoubtedly concerning every industry. Since the transportation sector releases one-third of global carbon emissions, offsetting vehicle emission is a substantial milestone in the net-zero emissions target [1]. Electrification of transportation contributes to uncontaminated air and less noise pollution in the urbanized area [2]. Since electric vehicles (EVs) emit 50% less CO2 than conventional vehicles (vehicles having internal combustion engines), the EV industry has gained significant importance recently. Also, if EVs are charged by cleaner energy sources, such as hydro, wind, and sun, the driving emissions will reduce dramatically [3]. Another way of reducing the overall emissions of EVs is by increasing their efficiency and life cycle. As an essential element that needs to be considered while mentioning efficiency, batteries undoubtedly change vehicles' characteristics drastically owing to their significant effect on their power output, driving range, and lifespan.

When EVs' power density, longevity, and efficiency need are considered, Lithium-ion batteries are the most suitable candidates for vehicular applications [4]. A case in point is that Li-ion batteries have greater power density and charging efficiency when compared with other battery types, such as NiMH, NiCad, and Lead Acid [5]. Also, since electric vehicles can recharge batteries by regenerative braking, they require batteries that can work under sporadically changing currents without getting harmed. To sum up, EVs require batteries with low self-discharge rates and high energy density and batteries that have not suffered from the memory effect [6].

However, likewise other power sources, Li-ion batteries face some safety and longevity issues related to their working conditions. The most critical drawback of Li-ion batteries is thermal management since there are numerous detrimental effects for operating temperatures lower than 20 ℃ and higher than 40 ℃, as the former increases the risk of dendrite growth and it decreases available battery capacity, and the latter increases ageing effects and it leads to lethal situations such as thermal runaway and explosion [7]. Additionally, battery packs of EVs involve numerous batteries working together. Since the available capacity of batteries varies with temperature, batteries in a

pack must operate at approximate temperatures to avoid the risk of overcharge and discharge. Similarly, ageing is another phenomenon affected by temperature. Therefore, acquiring uniformly ageing cells in a battery pack is crucial to avoid overcharged and discharged batteries during their service life [8]. Furthermore, overcharging and over-discharging have remarkably harmful effects on cells, the former causes lithium dendrite growth and the latter decomposes the anode current collector [9]. For these reasons, providing uniform temperature distribution is another crucial achievement, thus 5 ℃ is the safest maximum temperature range in a battery pack [8], [10].

Due to high currents and dense packaging, vehicle batteries generate a significant amount of heat that will raise the temperature to dangerous levels. Therefore, heat dissipation is crucial to EVs to keep the vehicles safe and efficient. To avoid the risk of thermal runaway and increase the cycle life of batteries inside the pack, the battery pack requires Battery Thermal Management Systems (BTMS), which dissipate the heat and keep the cells in a safe temperature range, decrease the temperature differences among cells working together, prevent dramatically changing temperatures, and ensure that the cells' internal temperature distribution is uniform. Pesaran [11] introduced certain types of BTMSs and defined their features and limitations. Overall, BTMSs can be classified based on their cooling techniques, namely passive and active cooling. Air cooling, direct liquid cooling, and indirect liquid cooling are active methods; and heat pipes, phase change materials (PCM), and natural convection conditions are considered passive methods. There are also different hybrid systems combining active and passive methods. Ultimately, each method is unique as they have certain positive and negative aspects regarding the system.

Passive cooling strategies are favourable as they do not consume power to provide cooling. Cooling with heat pipes rejects the heat efficiently, and as they can be manufactured in several shapes, space efficiency is another upside [12]. Also, they work well even if there is a slight temperature gradient, and their maintenance and lifecycle are favourable [13]. However, the systems with heat pipes are heavy and expensive. Additionally, numerous studies focused on thermal management with PCMs, another passive cooling method, as they can accumulate and release considerable amounts of heat owing to the latent heat capacity of PCMs [14]. The PCM stabilize the temperature during the operation; for this reason, they work well in cold environments. However, PCM's low conductivity makes the dissipation of accumulated heat harder. Therefore, they cannot cool the pack for a long time. Also, volume differences between solid and liquid states,

pollution rates, flammability, and safety are other concerns when considering a PCM application for EVs [15].

As for the active systems, direct and indirect liquid cooling methods reduce the maximum temperature more than air cooling methods, owing to their coolant's high thermal conductivity and heat capacity. Regarding the temperature range, on the other hand, air cooling keeps the cells in close temperature ranges when compared to liquid cooling methods [16]. However, the issues related to temperature are not the only aspects of BTMSs when evaluating their compatibility with EVs. Thus, their parasitic power need, complexity, manufacturability, and cost efficiency must be considered. In this regard, indirect liquid cooling systems require additional structures to avoid fluid leakage, which increases system complexity, weight, and cost. Also, leakage is a severe problem for battery packs as it leads to severe consequences, such as short-circuiting, thermal runaway, and explosion. Besides, air cooling mechanisms offer the most straightforward designs, and since they do not require an additional jacket or plate, their weight is relatively low. Additionally, the absence of extra structures makes maintenance cheap and easy and reduces manufacturing costs [12]. To sum up briefly, when all the features of air-cooled mechanisms are considered, they are suitable for small battery packs with lower power output [13].

In the air-cooled BTMS literature, many studies have focused on improving cooling performance by changing design features. The improvement can be done by changing the manifold design [17], battery positioning [18], [19], and flow characteristics [20], [21]. Also, there are several examples of adding different structures to direct or disturb the airflow [22], [23]. However, even though the baffles are universal structures used in the heat exchangers, there is a significant lack of academic studies on using flow disturbing structures between the batteries. This study documented the effects of flow-disturbing structures of different sizes and shapes on the cooling performance of battery packs. Several structures are placed near the batteries with higher temperatures to reduce the temperature gradient between cells and maximum temperature. Initially, a commercial Lithium-ion cell was discharged under several discharge rates to use the data for validating the electrochemical-thermal particle insertion battery model that was invented on the work of Fuller et al. [24]. Then, the battery module simulation was employed by coupling it with the single battery model. In addition, a battery module was manufactured from plexiglass, and experimental results were compared with the simulation. Finally, the thermal performance of various designs was evaluated by comparing their maximum

temperature, temperature gradients, fan power consumption, and volumetric power density of modules.

The sections of this thesis follow this outline; Lithium-ion batteries in the electric vehicle sector and remarkable battery thermal management systems from the literature are discussed in Chapter 2. Chapter 3 explains the mathematical model and experimental methods of this work. Chapter 4 displays all results obtained from the study, such as experimental results, validation of simulations, and thermal performance data in detailed tables, figures, and graphs. Finally, Chapter 5 summarizes the entire study and emphasizes the primary outcomes.

CHAPTER 2

LITERATURE REVIEW

In this chapter, the discussion is initiated by battery types and features of Lithium-ion battery chemistries. Consecutively, the thermal issues of Lithium-ion batteries and their outcomes are exemplified. Ultimately, after explaining the significance of battery thermal management systems (BTMSs) in electric mobility applications, the leading-edge designs of cooling systems in the literature are shown.

2.1. Batteries in Electric Vehicles

Many batteries are used in EVs and HEVs, such as nickel-cadmium (NiCad), nickel-metal hydride (NiMH), lead-acid, and Lithium-ion. It is well known that the electric vehicles' (EVs') efficiency, cost, and lifespan correlate with the same features as batteries [11]. Therefore, Lithium-ion batteries are the best candidates for vehicular applications compared with the other types [5]. The main concerns for commercial vehicles are maintaining the highest capacity with the lightest batteries and the ability to be fast-charged as the extension of charging time is directly proportional to capacity. Since the energy density of Lithium-ion batteries is at least two times higher than the others, the battery packs with Lithium-ion batteries offer the lightest pack with the highest power output thanks to the chemical properties and lightweight of Lithium metal. Another Lithium-ion battery feature favourable for EV applications is low self-discharge rate and longer life span [25]. These characteristics depend on the cathode material of batteries.

Even though many cathode materials can be used in Li-ion batteries, only several chemistries have been commercialized as safety issues and internal stability hamper the process [26]. Each cathode material has unique features that affect the efficiency, safety, price, and life cycle of batteries. In Table 2.1, the properties of commonly used cathode materials are documented.

Table 2.1. Characteristics of the common cathode materials [4], [26]–[28].

Cathode	NCA	NMC	LCO	LFP	LMO	LNO
Nominal Voltage	3.7V	3.7	3.9V	3.4	3.7	3.8
Cycle Life	-	2000	500	2000	1000	1200
Energy Density (Wh/kg)	280	200	155	160	120	275
Thermal Runaway (ºC)	200	210	150	270	250	<200
Safety	Moderate	Good	Poor	Excellent	Average	Poor
Price	Low	Moderate	High	Moderate	Low	Low

The first commercialized chemistry was LCO, and it is not favourable because of its unstable internal structure, high price, and short life span. On the other hand, LFP batteries are a common type for EVs since they provide safety and efficiency at reasonable prices. However, its power output is slightly lower than others; thus, they are not favourable for high C-rates. In addition, NCA is popular among EV producers as they are thermally stable because of the Aluminium compound. Also, the NCA cathode offers high capacity with fast charge/discharge capability. Nevertheless, Lithium-ion batteries suffer from thermal issues that can cause hazardous consequences or reduce their efficiency. While some cathodes (NCA, LFP, and NMC) can operate in a wide range of temperatures due to thermal stability, others are more sensitive to the operating temperature [26].

2.2. Thermal Issues in Lithium-ion Batteries

Since the temperature affects both efficiency and safety of operation, thermal issues are significantly important in the battery sector. Lithium-ion batteries can sustain within the temperature range of -40ºC–60ºC, but an effective operation requires an operating temperature range narrower than that [29]. Even though optimum operational temperature ranges change based on cathode material, the temperature range that Lithium-ion batteries (LIBs) work safe and efficient is approximately 15–35 °C [30].

Temperatures below 20 degrees obstruct the ion transfer inside the battery as the viscosity of electrolyte increases at low temperatures, which degrades the available capacity and state of charge [7]. Also, since the ions cannot intercalate appropriately at cold temperatures, lithium plating occurs on the anode surface, causing dendrite growth

[31]. If the dendrites reach the cathode, the internal short circuit occurs, which leads to thermal runaway [32]. Operating at temperatures higher than 40ºC accelerates the side reactions, which causes capacity fade and aging [7]. In figure 2.1, how available capacity degrades at various temperatures is displayed.

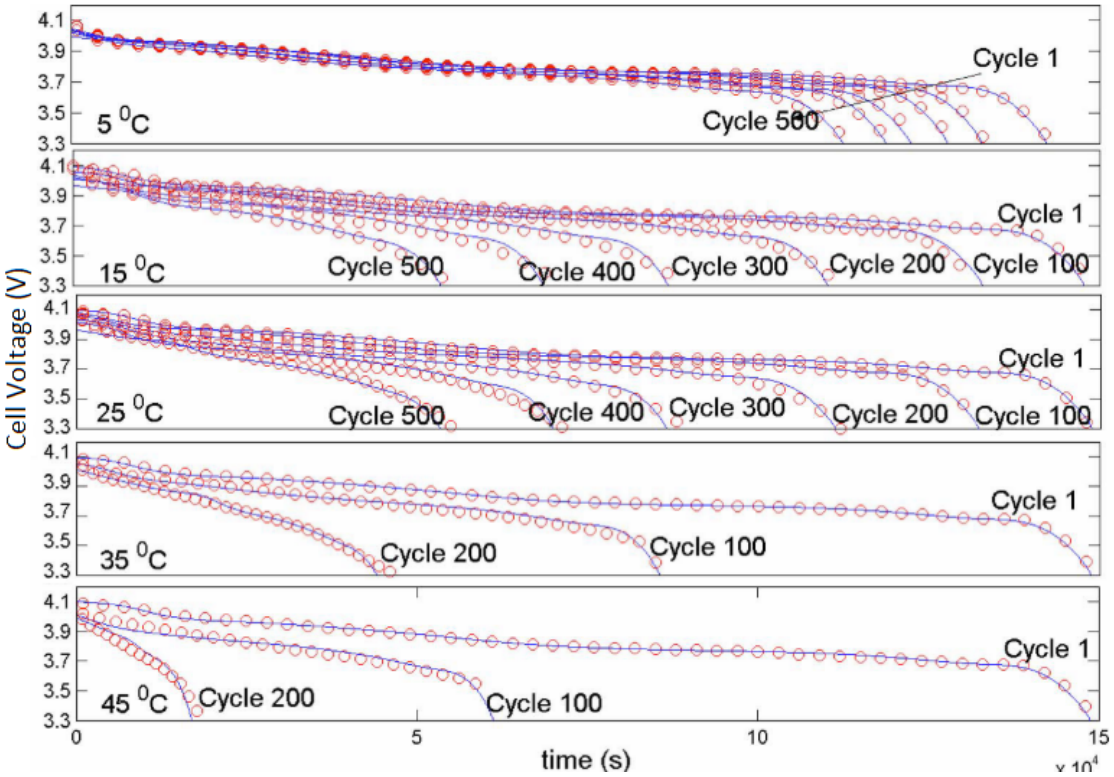

Figure 2.1. Comparison of capacity retentions under different temperatures [33].

It can be observed from the figure that available capacity increases for high temperatures, which can be seen by comparing the duration of the first cycles of 45ºC and 5ºC. However, as the available capacity of batteries at high temperatures degrades fast, there is a trade-off between more capacity and a longer lifespan. Furthermore, temperature dependency of aging rate and usable capacity obligates the regulation of temperature uniformity to avoid over-charged and over-discharged cells in a battery pack [8]. Therefore, the desired temperature range is 5ºC for simultaneously operating Lithium-ion cells [34].

In addition, thermal runaway is another issue induced by high-temperature operations, and it causes lethal consequences, such as explosion and fire [8]. Thermal runaway can be triggered by various reasons connected with poor thermal management, such as solid electrolyte interphase (SEI) film dissolution, an exothermic reaction

occurring after 70ºC [35]. Lithium-ion battery applications are notorious for thermal runaway, fire, and explosion incidents. These incidents include plane fires [36], mobile device explosions, and vehicle fires [37].

2.3. Battery Thermal Management Systems (BTMS)

To avoid the risk of thermal runaway and increase the cycle life of batteries, battery packs require Battery Thermal Management Systems (BTMS). The objectives of BTMS are keeping the cells in a safe temperature range by rejecting heat, decreasing the temperature differences among cells working together, preventing fluctuating temperatures, and ensuring that the cells' internal temperature distribution is uniform [11].

Table 2.2. Properties of various cooling mechanisms for BTMS [29].

		Advantages	**Disadvantages**
Passive	**PCM**	○ Cheap ○ Long life ○ Stable temperature distribution ○ High heat accumulation	○ Hard to dissipate accumulated heat ○ Leakage and pollution
	Air	○ Simple and light ○ Cheap ○ Easy maintenance ○ Zero parasitic power	○ Non-uniform temperature profile ○ Low heat rejection
	Liquid	○ Cheap ○ Easy maintenance	○ Leakage ○ Heavy
	Heat Pipe	○ High heat rejection ○ High efficiency	○ Complex ○ Expensive and heavy
Active	**Air**	○ Simple and light ○ Cheap ○ Easy maintenance	○ Non-uniform temperature ○ Parasitic power ○ Low efficiency
	Liquid	○ High heat rejection and heat capacity	○ Complex and heavy systems ○ Expensive ○ Hard to sustain ○ Leakage
	Peltier	○ No moving parts ○ Long life ○ Easy maintenance	○ Low heat rejection ○ High power consumption

Thermal management systems are divided into groups based on their cooling strategy, active and passive. Active systems involve an additional device to circulate coolant or provide heat rejection. Passive systems take advantage of natural processes like phase change and natural convection. Table 2.2 documents the upsides and downsides of each method. Although there are various solutions for thermal management, manufacturers prefer natural air-cooling for short-range vehicles, active air cooling for midsize vehicles, and indirect liquid cooling for high power and long-range vehicles [38]. There are also different hybrid systems, which combine active and passive methods. Many researchers focused on improving these techniques based on cooling performance, manufacturing and maintenance costs, pack complexity, and overall weight. These studies can be conducted numerically and experimentally.

2.3.1. Passive Methods

Passive cooling mechanisms aim at thermal management with natural processes, such as natural convection and latent heat. Since they do not require external devices, systems can run without consuming power, occupying space, and frequent maintenance cycles. Among the passive cooling methods tabulated in Table 2.2, phase change materials (PCMs) and heat pipes are the most popular methods in the literature. Cooling with phase change can happen as liquid-gas or solid-liquid changes. Phase change cooling with boiling liquid is generally done using dielectric coolants, which have superior cooling performance as the coolant directly contacts the cell surface.

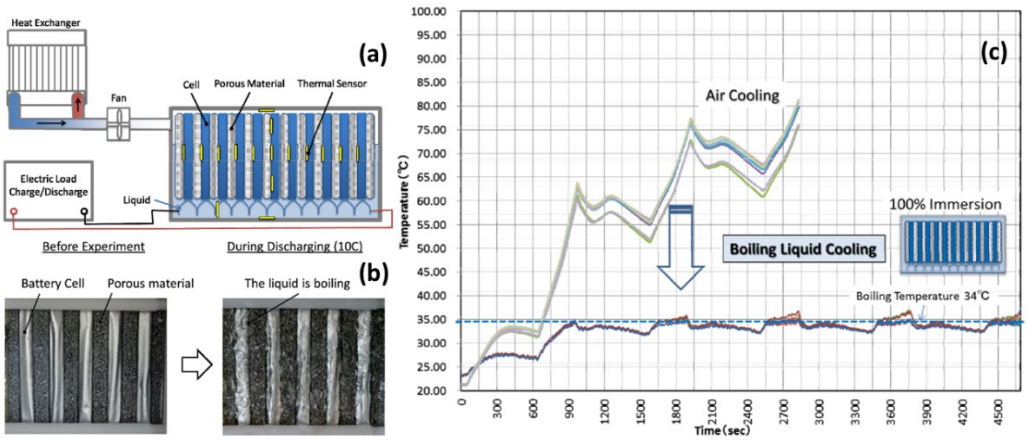

Figure 2.2. Experimental configuration (a), module image during 10C discharge (b), and temperature curves under 20C for air and liquid cooling (c) [39].

Hirano et al. [39] experimentally developed a two-phase liquid cooling system using hydrofluoroether as a coolant with a 34ºC boiling point temperature. They compared the results with the air-cooling method, and it shows excellent performance even under a 20C discharge rate. In Figure 2.2, the battery pack configuration and temperature curves under 20C discharge rate are given

It is clear from the figure that battery temperatures in air cooling rise to around 90ºC while two-phase liquid cooling keeps the batteries around the boiling point with little fluctuations. Similarly, Van Gils et al. [40] experimented on a single battery to assess the thermal performance of two-phase dielectric coolant liquid (Novec7000). They documented that the liquid could keep batteries at steady temperatures with slight fluctuations even though the boiling process does not emerge. Also, they reported that boiling could be intensified by decreasing the cooling chamber pressure. Figure 2.3 illustrates the experimental setup and temperature curves of the work.

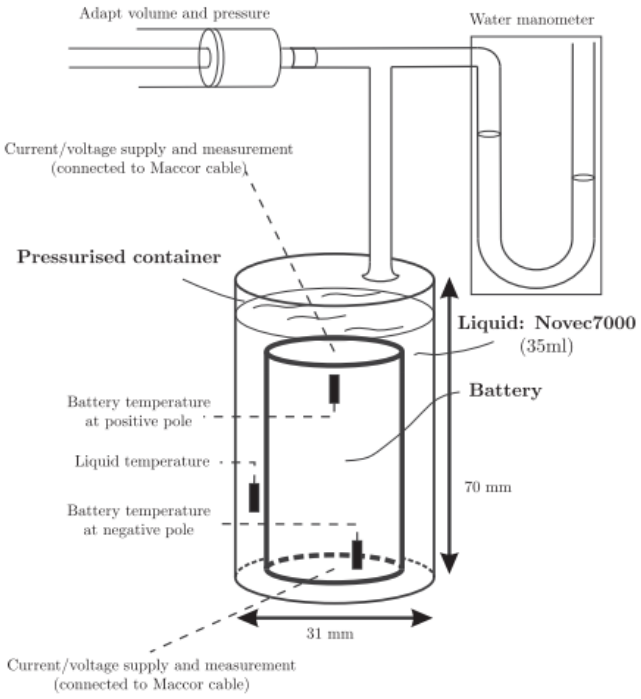

Figure 2.3. The diagram of the experimental setup in Val Gils' study [40].

They experimentally investigated the temperature profiles of two different external wall temperatures, 20ºC and 33ºC. Under a 5C discharge rate, the cell

temperature did not exceed 23 degrees while the wall temperature was 20ºC, and the cell temperature fluctuated around 34.5 degrees when the wall temperature was at 33ºC.

Along with the decent cooling provided by the two-phase liquid system, there are limitations to this method for EV applications. Firstly, as the boiling intensity directly relates to the temperature, the bubble formation starts restricting the heat dissipation for high temperature differences [41]. Secondly, such a mechanism is costly and complex since it requires hoses, evaporators, and a sturdy case. Due to the additional cost surged by a complex system, these systems are not yet applicable to the EV market, where manufacturers attempt to implement natural air-cooling systems to keep the prices in a reasonable range [38].

On the other hand, solid to liquid phase change cooling systems offer promising solutions to BTMS in EVs thanks to the simple designs with low prices. They provide a more uniform temperature with tiny fluctuations due to the latent heat of the phase change material. Additionally, researchers have focused on combining the PCM with active cooling systems and additive materials (metal foams, nanoparticles, and carbon compounds) to overcome the heat accumulation due to the low conductivity of the material. Hallaj et al. [42] numerically examined the thermal performance of a battery pack with eight cells submerged into PCM. They suggested that the surface temperature of cells cooled by PCM is almost 5ºC lower than the case without PCM. The temperature was uniformly distributed over the cell with PCM cooling. Also, they documented the thermal behaviour of cells during 24 hours of relaxation, proving the feasibility of PCM in cold environments. Karimi et al. experimentally investigated the effects of different additives (Cu, Ag, Fe_3O_4, and metal matrix) mixed with paraffin wax. As an effect of increased thermal conductivity, composite PCMs reduced the maximum temperature by 5ºC, and the maximum temperature difference of the system with metal matrix 7ºC lower than the paraffin. Lin et al. [43] conducted experimental and numerical solutions of a battery pack cooled with PCM impregnated carbon matrix and sheets. Figure 2.4 illustrates the experimental setup and diagram of this study. Their design successfully kept the batteries in the melting temperature range, almost 10ºC lower than the system without PCM. Also, the numerical simulation yielded good accuracy of a maximum 2% error between the experiment. Wang et al. [44] experimentally enhanced the thermal conductivity of PCM by placing various numbers of fin structures (2, 4, and 8). Even though last step temperatures for every finned design, the maximum temperature difference between the designs with 2 and 8 fins was around 10ºC. Regarding the last

time step data, the addition of fins reduced the maximum temperature by 6ºC. In Figure 2.5, the effect of fins on the melting process can be seen.

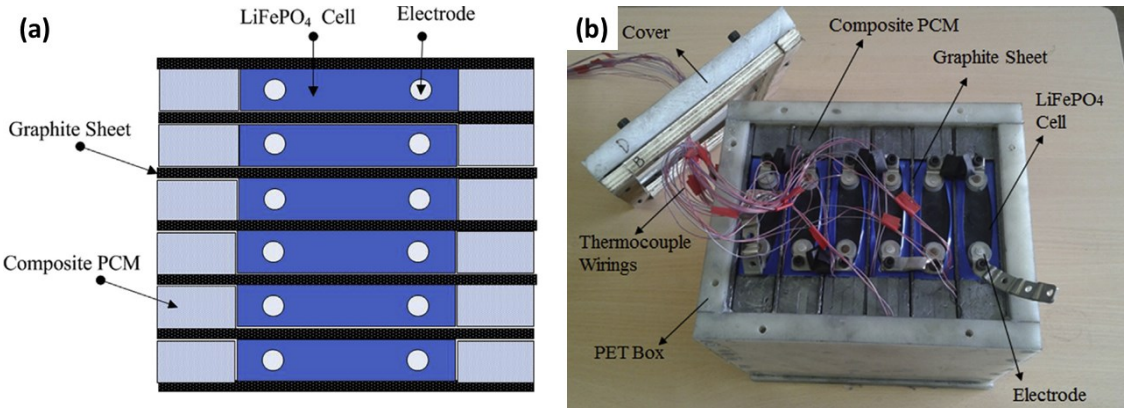

Figure 2.4. Pack diagram of PCM cooling system (a), experimental setup (b) [43].

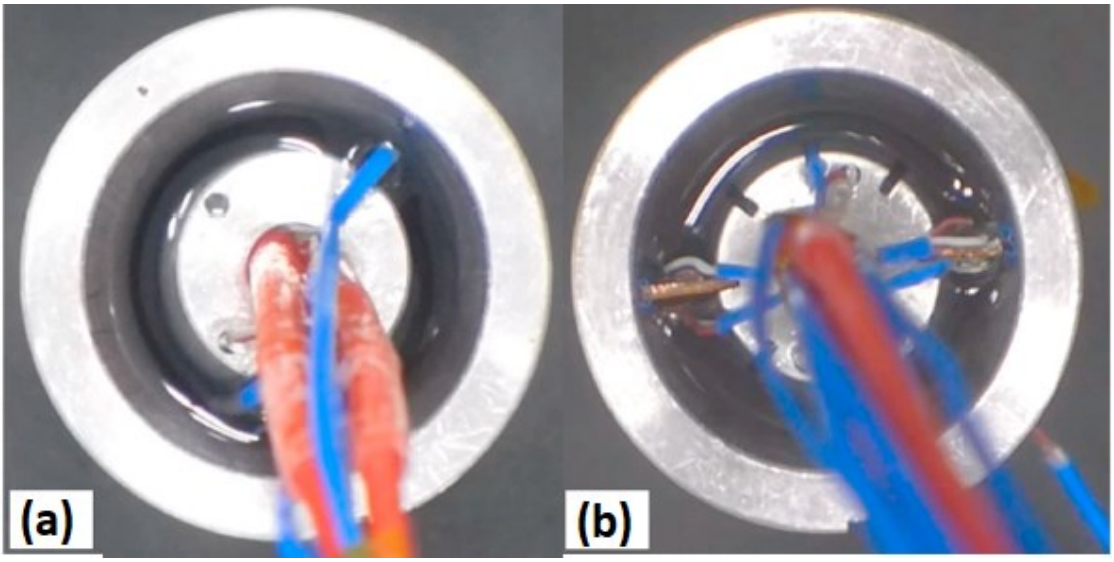

Figure 2.5. Molten PCM image of (a) no-fin design, (b) design with 2 fins [44].

It is clear from Figure 2.5 that while all the PCM is molten in the finned design, there is still a ring of solid PCM on the casing surface of the no-fin design.

In addition to thermal performance concerns of PCMs, flammability, pollution, and thermal expansion are other issues restraining the design processes [15]. In addition, to consider PCMs for automotive battery cooling mechanisms, the lifecycle, cost, and availability for mass production of the coolant are also essential.

Another essential element of passive thermal management is heat pipes due to their compactness and significant heat rejection rate under slight temperature differences. Heat pipes dissipate heat over liquid-gas phase change [45]. Since heat pipes do not require any maintenance and their lifespan is long, they are favourable for BTMS applications in EVs [46]. Liang et al. [47] studied heat pipe thermal management systems under various ambient conditions and intermittent coolant pumping. They documented that the system's performance is unchanging if the coolant temperature is between 25ºC–35ºC. Also, the cooling system can start operating after a specific threshold temperature that changes with ambient conditions is reached to balance the energy consumption. Figure 2.6 illustrates the experimental diagram of their study.

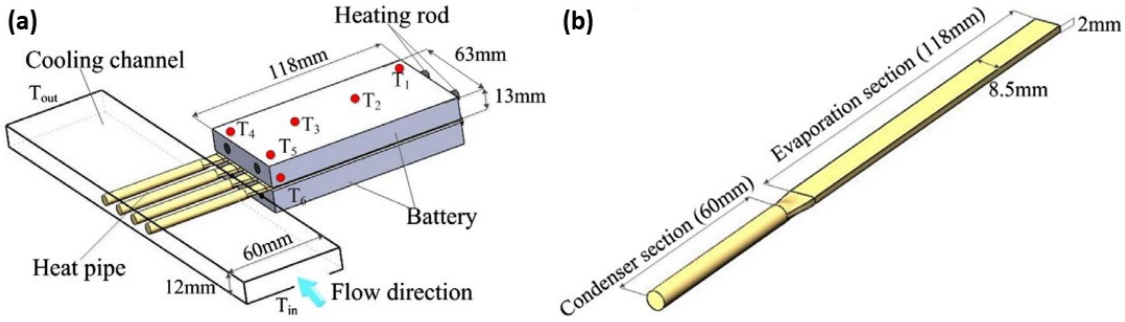

Figure 2.6. Experimental setup diagram (a) and the illustration of heat pipes used in the experiment [47].

Similarly, Zhao et al. [48] combined PCM filled battery pack with heat pipes cooled by forced air convection. They investigated the system's performance by comparing it with sole PCM and natural air-cooling conditions. As shown in Figure 2.7, the system comprises 12 batteries inserted into PCM, and heat pipes, whose condenser parts have fins, were placed between batteries. The results showed that the maximum decline in temperature gradient was 50% compared to natural air-cooling conditions. Also, the ultimate design reduced the maximum temperature of the system by 25% compared with the natural convection.

As for the disadvantages of heat pipe cooled BTMS, they are expensive and heavy systems. Heat pipe integrated systems are not space-efficient despite their high heat flux. Also, the application of heat pipes to EV thermal management is restricted by their low efficiency and narrow contact surface [13].

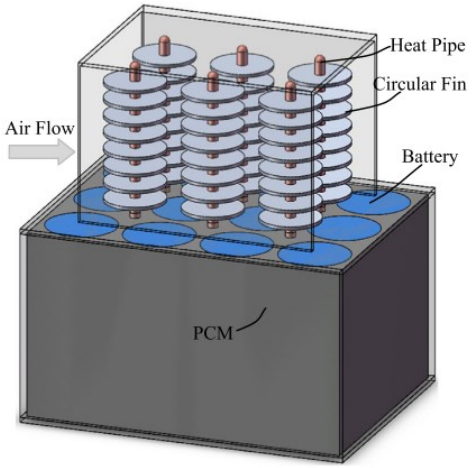

Figure 2.7. The experimental diagram of heat pipe, PCM, and air cooling combined system [48].

2.3.2. Active Methods

Active methods involve an external device (pump or fan) to circulate the coolant or heat transfer devices, such as thermoelectric coolers. Since they are more efficient and controllable than passive methods, the general interest of the EV market is active methods, especially air and indirect liquid cooling.

2.3.2.1. Forced Air Cooling

Air cooling is preferred due to its lightweight packs, simple designs, cheap manufacturing, and easy maintenance [12]. However, because of the lower heat capacity and thermal conductivity of air, the cooling performance of these systems is not efficient for higher C-rates. Hence, air cooling applications are favourable for EVs with short-range and lower power output [25].

Air-cooled BTMS literature focuses on optimising parameters to enhance the cooling performance and temperature uniformity. This enhancement can be divided into three groups. Flow characteristic involves velocity changes and fan operation changes. Manifold design optimizations refer to inlet and outlet placements, manifold shapes, and angles. Cell organization implies cell alignments, distances, and the addition of structures.

2.3.2.1.1. Changing Flow Characteristics

When the limitations arising from the low thermal conductivity and heat capacity of air are considered, cooling optimizations by changing the airflow is a mandatory option as it compensates for the lack of heat capacity. However, these alterations have limitations, such as pressure drops, power consumption, and noise [49]. Sabbah et al. [50] made comparisons between the phase change material (PCM) and the air cooling for a pack consisting of 20 cells (4S5P) under several discharge rates up to 6.7C. They documented that airflow was not adequately cooling the batteries when the ambient temperature was 45°C regardless of increasing Reynolds numbers. Mahamud et al. [20] adopted a novel airflow strategy where airflow changed direction, and they changed cell spacings and flow arrangements, whose diagram is given in Figure 2.8 a. As a result, the new airflow method decreased the temperature gradient by 72%, and the contribution of cell arrangements to the cooling was 10%. Saw et al. [51] experimentally and numerically investigated the cooling performance of a battery pack with 24 cells cooled down with axial airflow. Increasing the parasitic power consumption to around 0.6W reduced the maximum temperature and temperature difference by 37% and 66%. Chen et al. [16] compared the cooling performances of air cooling, fin cooling, cold plate, and direct liquid cooling by looking at each method's battery temperatures and pressure drops. The results showed that air cooling consumes more power than others to provide identical cooling. Also, they found that while faster flow rates significantly reduced the maximum temperature, the effect of flow rate on temperature gradient was small. Yu et al. [52] experimentally assessed the axial air cooling method for a battery pack with 66 cylindrical cells (3S22P) under lower discharge rates (0.5C-1C). They optimized the flow rate based on maximum temperature and temperature gradient. As it is clear from the above studies that alongside the power consumption, cooling performance limits the optimum flow rate as its effectiveness gradually decreases.

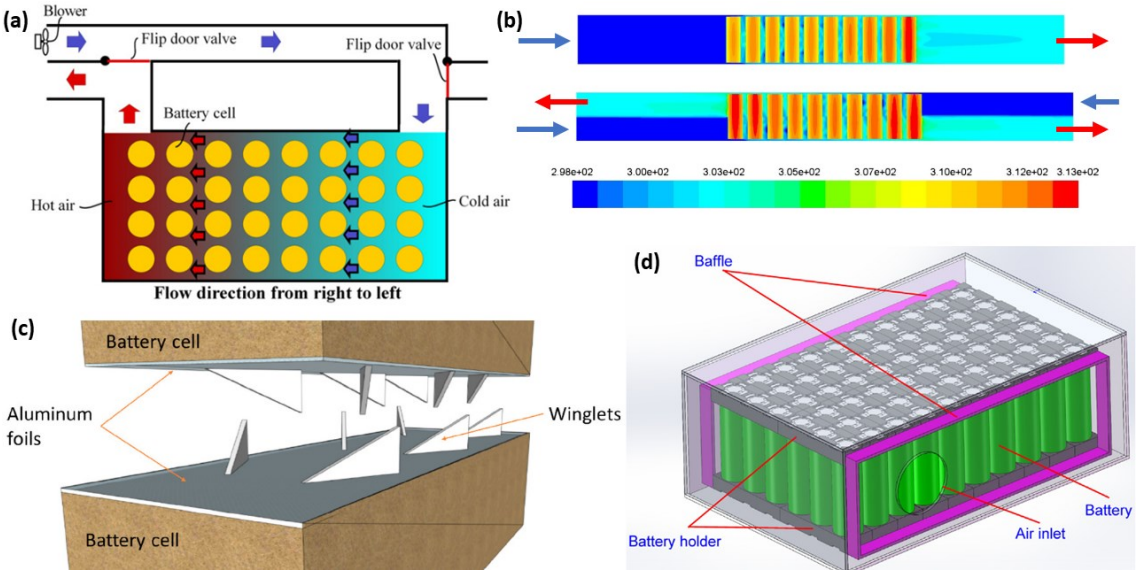

Figure 2.8. Illustration of reciprocating airflow design (a)[20], temperature contour (in K) of the work of Na et al. [53](b), heat transfer enhancement with winglet vortex generators on prismatic batteries (c)[49], and manifold design for cylindrical cells (d)[22].

2.3.2.1.2. Manifold Design Improvements

The alterations in manifold design are one option that is in favour of uniform air distribution among cells, as equally distributed air is another objective for air-cooled BTMSs [12]. Also, inlet and outlet repositioning significantly affect cooling performance [54]. Xie et al. [17] employed the orthogonal array testing technique to understand the effect of inlet/outlet widths and angles using numerical methods. They found the best option for inlet and outlet properties, which yielded a 13% lower maximum temperature and 30% better temperature gradient than the base design. Shahid et al. [23] extended the inlet to provide extra air to the hotspots by changing air direction with additional planes. They aimed to increase the heat transfer coefficient by enhancing turbulence. The best configuration was extending the inlet upwards and dividing the flow chamber halfway through the batteries on top. It yielded 8% better cooling with 25% more uniform temperature distribution than the base design. Na et al. [53] documented the cooling improvement with two inlets placed on various sides of the module whose air domain was divided into two parts with a grid, as shown in Figure 2.8 b. Results showed that inlets at opposite sides decreased temperature difference by 47% and maximum temperature by

2.7°C. Jiaqiang et al. [22] studied different inlet and outlet placements and the addition of baffles in a battery pack with cylindrical cells shown in Figure 2.8 d. They reduced the maximum temperature by 26% after placing the inlet and outlet on opposite sides and locating the baffles. Jilte et al. [55] placed each module in a discrete channel to compare its cooling performance with the base design without channels. They reduced the maximum temperature by around 18%. However, as channels reduce the temperature of the first cell more than the base design, they did not improve the temperature uniformity. Zhou et al. [56] developed a novel design in which they located perforated pipes between the cylindrical cells and injected the air through the holes in the pipes. They managed to keep batteries in a safe temperature range even under a 5C discharge rate.

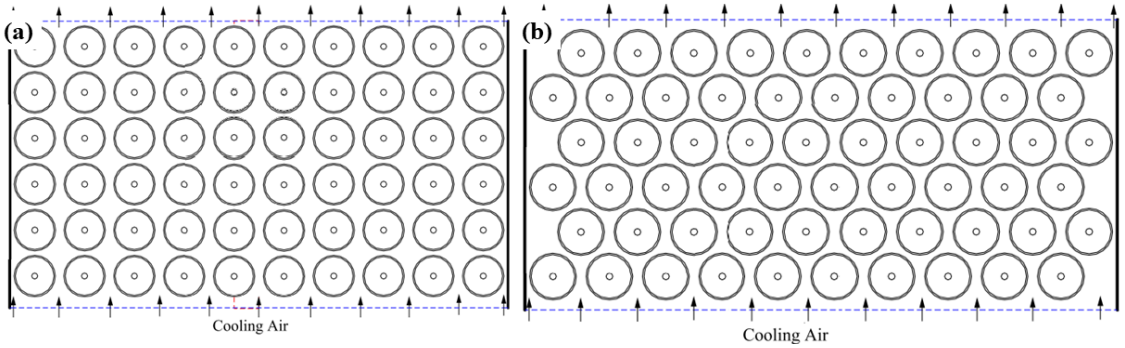

Figure 2.9. The diagram of inline (a) and staggered (b) designs of cylindrical batteries [57].

2.3.2.1.3. Battery Arrangements

Cell arrangements are necessary for acquiring volumetric power efficiency and cooling improvements. Also, while changing cell layouts, the pressure drop is another variable that needs attention. Gocmen et al. [19] optimized the mass flow rates between batteries using constructal theory [58] and compared the results with natural convection conditions. As a result, while forced air convection yielded 42% lower maximum temperature and 15% better temperature gradient than natural convection, the design with relocated batteries reduced the maximum temperature by 60% and temperature gradient by 97%. Yang et al. [18] evaluated the cooling performance of stagger and inline alignments and found the best spacings for both. The representative diagram for staggered

and inline alignments are displayed in Figure 2.9. They documented that the best design of inline kept the batteries in 0.9°C range with 34.55°C maximum temperature, that of staggered design yielded 33.8 maximum temperature with 1.2°C maximum difference. Lu et al. [59] investigated the cooling performance of a battery pack involving 252 cells cooled down with axial airflow. Increasing the Reynolds number reduced the maximum temperature by around 26%, while cell distance optimization decreased by 35%. Yang et al. [60] assessed the cooling effectiveness of a battery pack cooled with axial airflow by changing the flow rate and battery distances. The system acquired a 47% better temperature gradient and 16% lower maximum temperature with a loss of 27% space efficiency, and this design consumed 95% less parasitic power. Han et al. [49] numerically investigated the required volume flow rate of the battery pack in various scenarios, and they documented the effect of winglet parameters on the cooling of prismatic cells. As a result, they explained the limitations of air-cooling systems and the effectiveness of winglet vortex generators. Also, winglet placements on the cells can be seen in Figure 2.8 c.

2.3.2.2. Liquid Cooling

Liquid cooling is generally adopted by EVs having long-range and high power output due to coolant liquids' high heat capacity and thermal conductivity [12]. Liquid cooling methods have two categories based on the battery-coolant interface: direct and indirect. Direct contact cooling involves dielectric coolants, which directly touch the battery surface. Since there is no extra layer between coolant and battery, the cooling performance of dielectric liquids is 2.5-3 times more effective than cold plate techniques [61]. Also, dielectric liquids are far safer than water-glycol mixtures, as water can lead to disastrous results in case of leakage, and dielectric liquids are less contaminating than the water-glycol mixture. As for the disadvantages of dielectric fluid immersion cooling (DFIC) systems, their corrosive effects necessitate additional material research for sealing components, tubes, and casing. In addition, dielectric coolants used in direct cooling methods can be contaminating and flammable, and they are also expensive and heavy when compared to indirect liquid cooling.

On the other hand, indirect liquid cooling uses water as a coolant, and its thermal performance can be increased by additives, such as glycol, ethylene, and nanoparticles.

Also, indirect cooling methods offer outstanding efficiency due to water's high heat capacity and thermal conductivity. Nevertheless, they suffer from leakage problems, low thermal conductivity, and parasitic power consumption [62].

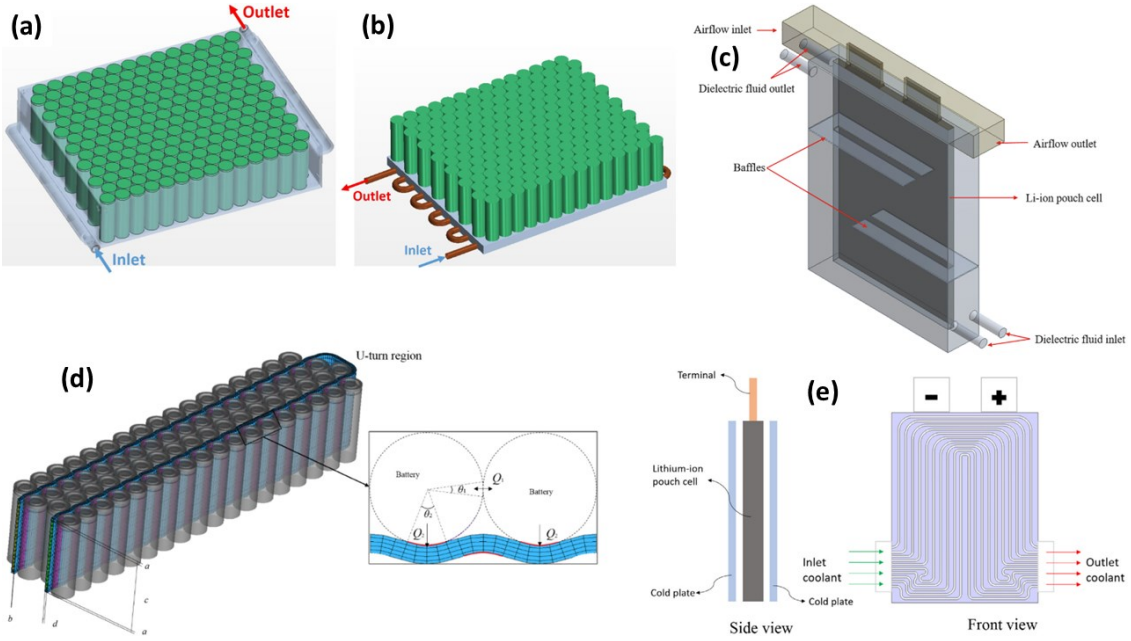

Figure 2.10. DFIC setup for battery pack with cylindrical cells (a)[61], cold plate cooling mechanism for the same pack (b)[61], the diagram of immersion liquid and air cooled tabs combined system (c)[63], indirect water-glycol system with wavy channels between cylindrical batteries (d)[64], cold plate cooled pouch type battery diagram (e)[65].

The direct liquid cooling literature has many gaps, such as the longevity of coolant liquids, the most proper coolant for EV applications, safety issues and mitigation methods, and design improvements for EVs [41]. Dubey et. al [61] numerically investigated the cooling efficiency of a battery pack consisting of cylindrical cells that cooled with dielectric liquid by comparing it with the cold plate cooling performance of the same pack. The pack designs are displayed in Figure 2.10 (a-b). According to their results, even though immersion cooling demonstrates good cooling performance in maximum temperatures, it cannot provide good uniformity. However, by optimizing the flow path of the coolant, this condition can be prevented. Besides, Suresh et. al [63] studied the thermal performance of immersion cooling combined with an air-cooled tab region, and they stated that DFIC combined with air cooling executes 46% better

performance than natural convection. Figure 2.10 (c) shows the diagram of the experimental setup used in the study.

Similarly, Sundin et al. [66] experimentally compared a prismatic Li-ion cell's cooling performance under forced air cooling and DFIC. They discovered that DFIC provides 5ºC lower temperatures than air, and the temperature fluctuation range over a cycle of DFIC and air-cooling methods were 5ºC and 16ºC, respectively. Ultimately, while designing a DFIC system, several objectives, including material investigation, effects of different coolants, design options and improvements, and cost and production investigations, should be considered.

Alongside air cooling and direct liquid cooling methods, there are various examples of indirect water-cooling methods in both the literature and EV market. Due to its remarkable thermal performance, water cooling methods are of general interest to BTMS applications for EVs and HEVs. Panchal et al. [67] investigated the performance of the cold plate water cooling mechanism of a prismatic Li-ion cell for different discharge rates, and as a result, the highest temperature profile is observed while inlet temperature is 35ºC and 4C is discharge rate, which is approximately 45 ℃ at tab region. Another study done by Patil et. al [65] involves cold plate cooling method optimizations for various discharge rates. The front and side views of the cold plate system are shown in Figure 2.10 (e). As a result, they found a flow pattern that can keep the maximum cell temperature and temperature difference below 40 ℃ and 1 ℃ respectively.

Additionally, Zhao et. al [64] investigated the thermal behaviour of wavy channels between cylindrical cells, resembling the system used in Tesla cars (Fig. 2.10 d), and results demonstrated that the system could keep the maximum temperature and temperature difference below 40 ℃ and 5 ℃ for 5C discharge, respectively. However, as it can be interpreted from these studies, despite the effective cooling performance and uniform temperature distribution of water-cooling mechanisms, they have safety issues caused by the electrical conductivity of water. Also, water-cooling mechanisms require additional structures to avoid fluid leakage, which increases system complexity and cost.

2.3.3. Hybrid Methods

Generally, BTMS literature involves many examples of thermal performance enhancements done by design improvements, as explained in the former sections.

Another technique of such enhancement is combining the methods to overcome each one's downsides. This hybridization can be made by combining two active systems or active and passive systems; the active-active combinations are ineffective as the parasitic power consumption increases. However, active-passive combined systems are the focus of the literature. For instance, although PCMs have good features, their applications are not viable without enhancing the thermal conductivity and heat dissipation [68]. Qin et al. [69] experimentally documented the thermal performance of active air and PCM cooled battery packs, as shown in Figure 2.11 (a). Compared with the passive method, the hybrid system decreased the maximum temperature and temperature gradient by 16ºC and 1.2ºC, respectively. Also, they created a numerical model of the same design to improve its parameters, and they suggested that 5mm is the optimum cell-to-cell distance. Wu et al. combined PCM and heat pipes cooled by forced airflow, and they experimentally investigated its cooling performance. Figure 2.11 (b) shows the diagram of this study. They compared the results of modules with only heat pipe, only PCM, and PCM-heat pipe combination. As a result, under a 5C discharge rate, while only heat pipe or PCM designs exceeded 50ºC, the heat pipe and PCM combination kept the temperature under 50ºC.

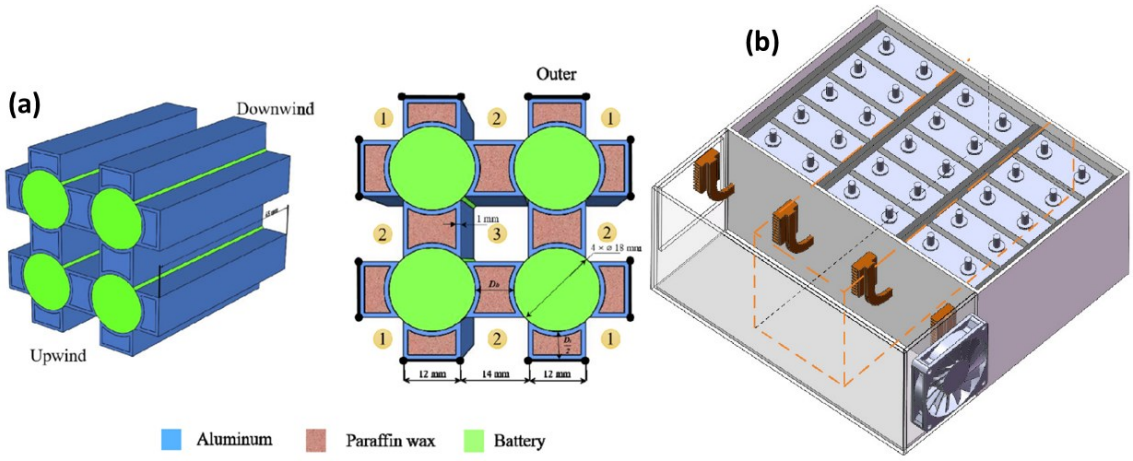

Figure 2.11. Forced air-PCM combined cooling design (a)[69], heat pipe assisted PCM BTMS (b)[70].

In conclusion, battery applications for EVs and HEVs require thermal management systems to operate safely and efficiently, and there are several methods for supplying thermal management. On the one hand, there are some goals all BTMSs methods must achieve in common, such as providing uniform temperature, offering sufficient heat dissipation, being lightweight and cheap, involving safety precautions in

case of accident or thermal runaway, and having less complexity. On the other hand, each novel technique designed for thermal management has typical problems that must be resolved.

CHAPTER 3

MATERIALS AND METHOD

In air-cooled BTMS literature, many studies focus on cooling improvements by optimizing cell arrangements, flow characteristics, and manifold designs. However, cooling improvements by additional structures were not assessed by many studies. Hence, this paper assessed the effect of several flow-disturbing structures, including vortex generators, on the cooling performance of a module consisting of 12 cylindrical Lithium-ion batteries. This study aimed to acquire a reliable simulation for a battery module including a dozen cells to enhance the cooling performance. For this purpose, experiments were conducted to validate both the battery model and battery module simulation. In the experiments, six batteries connected with the 2P3S layout were placed in a plexiglass module whose air was supplied by an AC fan. The simulations comprise 3D turbulent airflow and heat transfer coupled with 1D electrochemical-thermal battery model. While the stationary solver solved the flow field, the time-dependent solver solved the heat transfer and battery parameters in COMSOL Multiphysics 5.5. Inlet velocity and temperature were set to 1.6 m/s and 20 °C, and the initial temperatures of each component were same as the inlet. The cell is commercially available 21700 cylindrical Lithium-ion cell (capacity= 4200 mAh, maximum voltage=4.2V, and minimum voltage=2.5V) [71]. The battery dimensions are given in Table 3.1 with descriptions.

Table 3.1. Structural properties of the battery.

Parameter	**Value [m]**
Radius of battery (r_{batt})	1.05×10^{-2}
Radius of mandrel (r_{mand})	3×10^{-3}
Height of battery (h_{batt})	7×10^{-2}
Battery casing thickness (d_{can})	2.5×10^{-4}

Batteries were placed in staggered and inline alignments with 7mm and 15mm cell-to-cell distances. Also, different types of baffles (cylindrical, diamond, triangle, winglet) were placed between the cells for inline design. The design layouts of inline and staggered designs are illustrated in Figure 3.1.

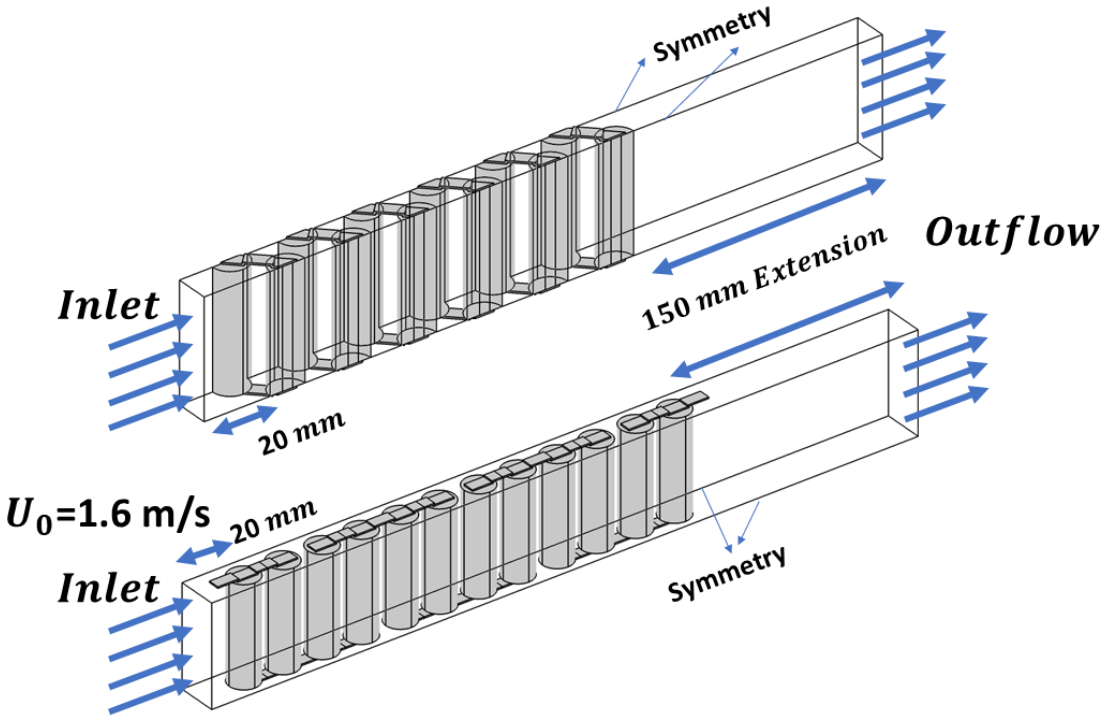

Figure 3.1. Illustration of simulations for (a) staggered design and (b) inline design.

3.1. Battery Thermal Model

Designing an accurate heat generation model for the cell is vital for BTMS studies. Therefore, an electrochemical-thermal coupled model was used. The electrochemical model of the battery comprises mass conservation, charge balance, heat generation, and electrochemical kinetics equations, which were defined by Fuller, Doyle, and Newman [24]. The work scheme of the multiscale P3D battery model is shown in Figure 3.2. The electrochemical part of the cell is designated as a 1D domain where ion flux occurs in x-direction, whose equations and boundary conditions are explained in Appendix A. To create a 3D model of the battery, an approach, namely pseudo-3D, was used. In the P3D model, the battery's internal structure is treated as a single material whose thermodynamic

properties are calculated by averaging all properties of battery materials as in Equations 6, 7, 14, and 15.

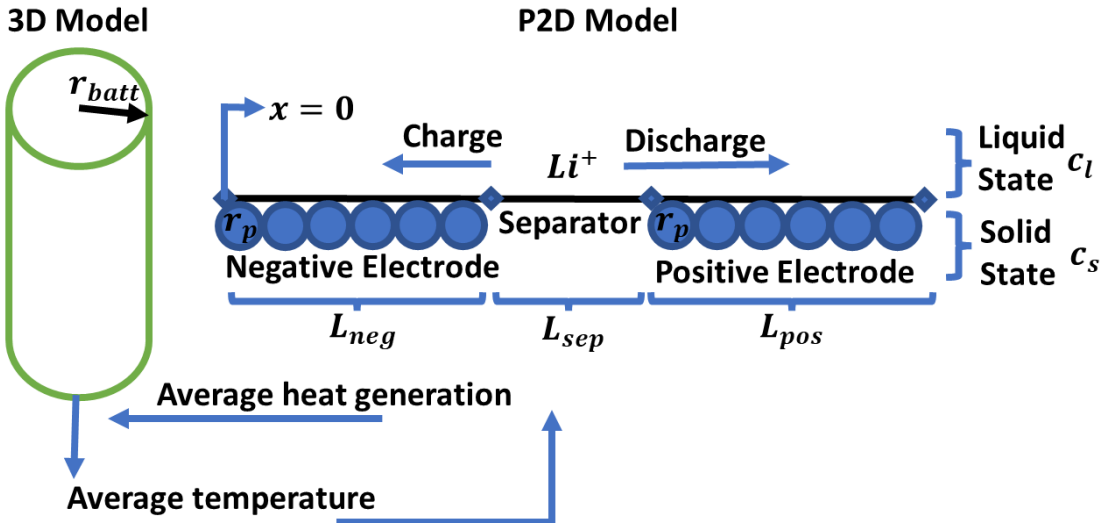

Figure 3.2. Illustration of P3D battery model with 1D and 3D domains.

Also, in the P3D model, heat generation is calculated as an average heat rate of the cell's active layers (anode, separator, and cathode), which was applied in the 3D model. Then, the volumetric average temperature of the 3D model was used as the temperature of the 1D model, as illustrated in Figure 3.2. The cell involves graphite anode, NCA cathode, and $LiPF_6$ solved in 3:7 EC/EMC as electrolyte. Aluminium and copper are the materials of negative and positive current collectors, respectively. All the material properties are given in Appendix A.

3.2. Governing Equations

The flow was designated as incompressible turbulent since the Reynolds number exceeded 4000 in the inlet region ($Re = {\rho_{air} U_0 D_{hydraulic}}/{\mu_{air}}$). The earlier studies used the k-ε turbulent model, and it showed good compatibility with simulations and experiments [18], [22], [60]. Hence, the k-ε turbulent model was adopted in this study. The governing equations are defined in the User's Guide section of COMSOL Multiphysics 5.5 [72]. The model is calculated as follows:

$$\rho(\nabla \cdot U)\varepsilon = \nabla \cdot \left[\left(\mu + \frac{\mu_T}{\sigma_\varepsilon}\right)\nabla\varepsilon\right] + C_{\varepsilon 1}\frac{\varepsilon}{k}P_k - C_{\varepsilon 2}\rho\frac{\varepsilon^2}{k} \quad (1)$$

$$\rho(\nabla \cdot U)k = \nabla \cdot \left[\left(\mu + \frac{\mu_T}{\sigma_k}\right)\nabla\mathrm{k}\right] + P_k - \rho\varepsilon \quad (2)$$

Where ε and k stand for the dissipation rate and turbulent kinetic energy respectively. The turbulent viscosity (μ_T) is calculated as in Equation 3, and the turbulence production (P_k) is calculated by Equation 4.

$$\mu_T = \rho C_\mu \frac{k^2}{\varepsilon} \quad (3)$$

$$P_k = \mu_T\left[\nabla U : (\nabla U + (\nabla U)^T) - \frac{2}{3}(\nabla \cdot U)^2\right] - \frac{2}{3}\rho k \nabla \cdot U \quad (4)$$

The boundary conditions (BCs) and initial conditions (ICs) of the problem can be described as follows:

- **Inlet:** The air properties are: $U_0 = 1.66\ m/s$ and $T_{inlet} = 20\ °C$.
- **Outlet:** The temperature gradient in the flow direction and pressure are zero at the outlet region.
- **Walls:** No-slip boundary condition at walls, and top and bottom walls are insulated.
- **Initial Conditions:** The temperature of the entire system is 20°C initially.
- **Symmetry:** Symmetry boundary conditions were attained to the side surfaces, as shown in Figure 3.1.

The model constants for turbulent flow are given in Table 3.2. The energy balance of a cell is described as:

$$\rho_{batt} Cp_{batt}\frac{\partial T}{\partial t} = (k\nabla T) + Q_{tot} \quad (5)$$

The first term in the right-hand side of Equation 5 defines the heat rejection between batteries and ambient. Where ∇T stands for the difference between battery

surface and coolant temperatures. The parameter k is the conjugate heat transfer coefficient. Heat transfer of the single battery model was designated as free convection, whose value is 6 $\frac{W}{m^2K}$. Forced convection was the heat transfer method of battery module simulations, and its heat transfer coefficient was changing based on the flow characteristics near the cells. Also, ρ_{batt} and Cp_{batt} are the bulk properties of active material, which are calculated as follows:

$$Cp_{batt} = \frac{\sum_i L_i Cp_i}{L_{batt}} \tag{6}$$

$$\rho_{batt} = \frac{\sum_i L_i \rho_i}{L_{batt}} \tag{7}$$

Where the subscript i changes for current collectors, anode/cathode, and separator. There are distinct sources of internal heat generation of a battery, and they can be divided as in Eq. 8.

Table 3.2. Model constants of the turbulent flow model.

Constant	**Value**
C_μ	0.09
$C_{\varepsilon 1}$	1.44
$C_{\varepsilon 2}$	1.92
σ_ε	1.3
σ_k	1.0
U_0	1.66 m/s
p_0	0

$$Q_{tot} = Q_{rev} + Q_{irr} + Q_{ohm} \tag{8}$$

Reversible heat generation (Q_{rev}) stems from the potential change of electrode with temperature, also called entropic heat generation. Irreversible heat generation (Q_{irr}) occurs due to the over-potential demand of chemical reactions. Ohmic heat (Q_{ohm}) is

generated due to the potential differences between solid and electrolyte domains. All heat generation terms are described in the following equations:

$$Q_{rev} = j^{Li+} T \frac{\partial E_{eq}}{\partial T} \tag{9}$$

$$Q_{irr} = j^{Li+}\left(\phi_s - \phi_l - E_{eq}\right) \tag{10}$$

$$Q_{ohm} = i_l\left(\frac{\partial \phi_l}{\partial x}\right) + i_s\left(\frac{\partial \phi_e}{\partial x}\right) \tag{11}$$

$$i_l = \left(\kappa^{eff}\frac{\partial \Phi_l}{\partial x} + \frac{2RT\kappa^{eff}}{F}(t_+^0 - 1)\left(1 + \frac{d\ln f_{\pm}}{d\ln c_l}\right)\frac{\partial \ln c_l}{\partial x}\right) \tag{12}$$

$$i_s = \sigma_s^{eff}\frac{\partial \Phi_s}{\partial x} \tag{13}$$

Where i_s and i_l correspond to current density in solid and liquid phases respectively. Also, the thermal conductivity of jelly roll (the active part that generates heat) is calculated as in Equations 14 and 15.

$$k_r = \frac{L_{batt}}{\sum_i \frac{L_i}{k_i}} \tag{14}$$

$$k_z = k_\theta = \frac{\sum_i L_i k_i}{L_{batt}} \tag{15}$$

The heat generation term is corrected as in Equation 16 before attaining it to the model. On the right-hand side of Equation 16, the first term describes the average heat generation of anode, separator, and cathode. Therefore, the second term represents the fraction of heat-generating layers and total cell length. The third term expresses the ratio between the jelly roll and total battery volume.

$$Q_{tot,3D} = Q_{tot,1D}\frac{L_{neg} + L_{sep} + L_{pos}}{L_{batt} + L_{Al,cc} + L_{Cu,cc}}\frac{\left[(r_{batt} - d_{can})^2 - r_{mand}^2\right][h_{batt} - 2d_{can}]}{[r_{batt}^2 - r_{mand}^2]h_{batt}} \tag{16}$$

3.3. Experimental Setups

Two experiments were conducted in this study. Initially, a single battery was discharged with 0.1C, 1C, 3C, and 5C by an electronic load (BK Precision 8614), where the battery was in natural convection conditions with an ambient temperature of 20 ±1 °C. Temperature (by k-type thermocouples) and voltage data were collected with a data logger (Hioki HiLOGGER LR8431). With the data of the single battery experiment, a 1D electrochemical-thermal model of a cylindrical Li-ion battery with NCA cathode, graphite anode, and liquid electrolyte (Molicel 21700 INR P42A) was created by adopting some parameters from the literature and fitting several parameters based on the single battery discharge data acquired from experiments.

Another experiment was carried out to validate the module cooling simulation. First, a module was manufactured from plexiglass, and three layers of honeycomb structures were placed to mimic the air manifold characteristics in the application. In the experiment, 120mm×120mm AC fan supplied air to the 120mm×70mm module. The experimental setup is shown in Figure 3.3.

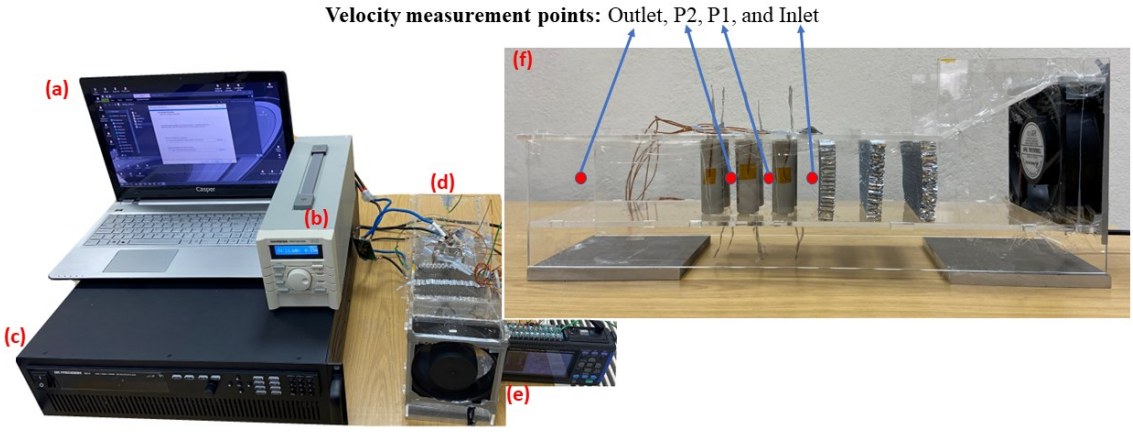

Figure 3.3. (a) Computer for data interpretation, (b) power supply (GW Instek PSH 2018a), (c) electric load (BK Precision 8614), (d) the module with fan, (e) data acquisition center (Hioki HiLOGGER LR8431), (f) experimental setup without connections.

In Figure 3.4, the distancing and how the batteries were located can be seen. For experiments and the simulation, the distances between batteries were set to S_T = S_L=10mm. During the experiments, batteries were discharged with 3C for 1086 seconds,

where the cut-off voltage was 2.5V. Both the pack voltage and a single cell voltage were measured and recorded during the experiment. Temperature values were measured from the middle surface of batteries with k-type thermocouples. In addition, the inlet air temperature was also measured during the experiment, and it was 20 ±0.5 °C.

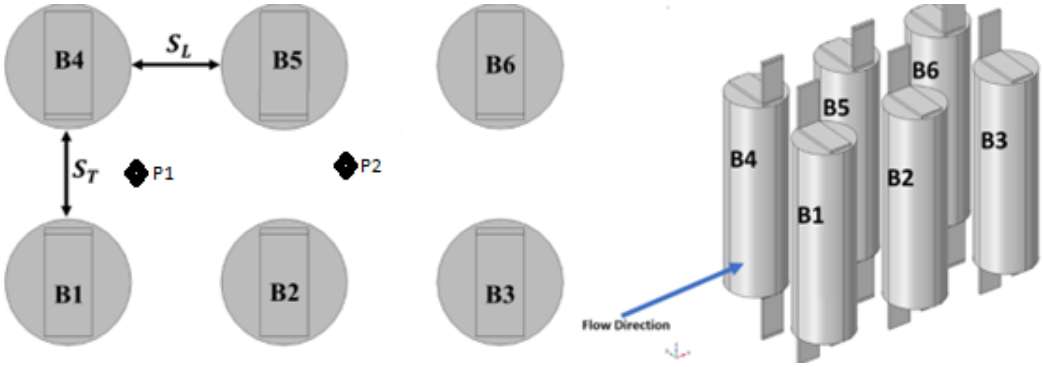

Figure 3.4. Design layout and dimensions, and air velocity measurement points.

3.3. Numerical Models

All numerical solutions were solved by COMSOL Multiphysics 5.5. The convergence criteria of turbulent flow were 10^{-4}, and that of battery simulation and heat transfer was 10^{-5} and 10^{-6}, respectively. While designing the pack simulation, turbulent flow k-ε, heat transfer in solids and fluids modules were coupled with the 1D Lithium-ion battery module in COMSOL Multiphysics 5.5. Electrochemical and thermal models were simulated in a time-dependent manner, whereas fluid flow was solved as a steady-state due to time-independent characteristics of the fluid flow in COMSOL Multiphysics 5.5 [73].

The single battery simulation was used to validate the battery thermal model, and it involves a cylindrical cell with busbars, as shown in Figure 4.1 (b). While solving the single battery model, $6\ \frac{W}{m^2K}$ of heat transfer coefficient was attained to the cell surface, which is an approximated value for natural convection on vertical cylinder surfaces [74]. The time step was taken as 1s while solving heat transfer and battery models with a segregated solver, which solves the battery equations given in Appendix A firstly and energy equations secondly.

The simulation of battery module validation had the same design parameters as the experiment. Six batteries were in the middle of the cooling channel of 120mm in width and 70mm in height. The inlet and outlet ports of the model were extended by 20mm and 150mm, respectively, to acquire developed flow characteristics during the solution. In Figure 3.5 simulation model and designated mesh structure are shown.

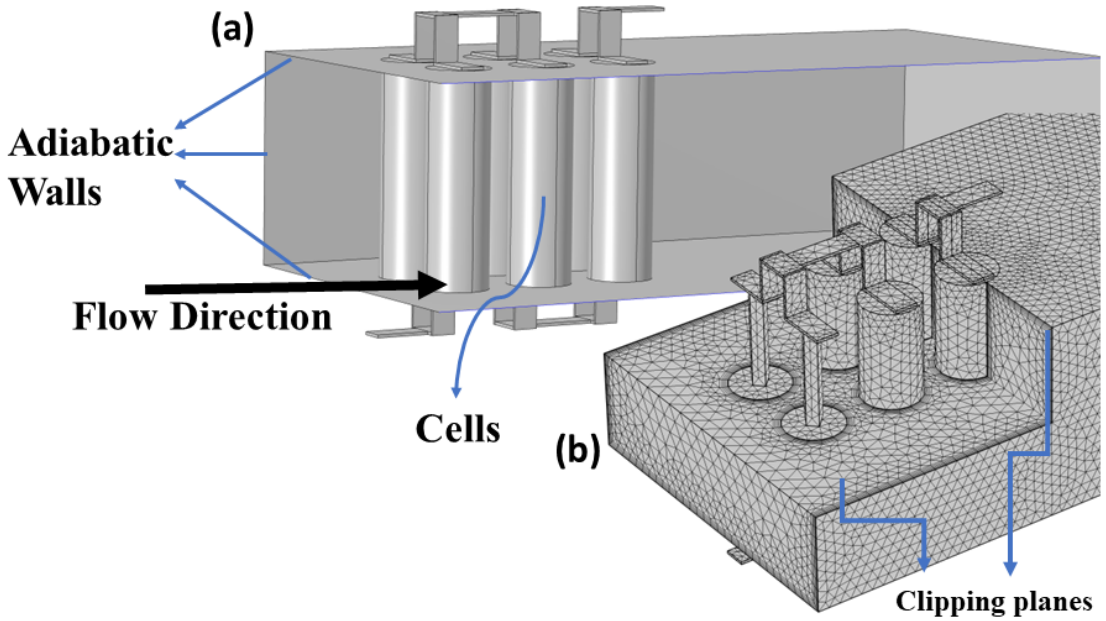

Figure 3.5. (a) 3D simulation model, (b) mesh structure (clipped for a clear view of internal mesh).

Lastly, all heat transfer enhancements were performed on a battery module simulation consisting of 12 batteries connected in a 2P6S arrangement. To save computational cost, symmetry boundary conditions were used. The design parameters of inline and staggered designs are illustrated in Figure 3.6.

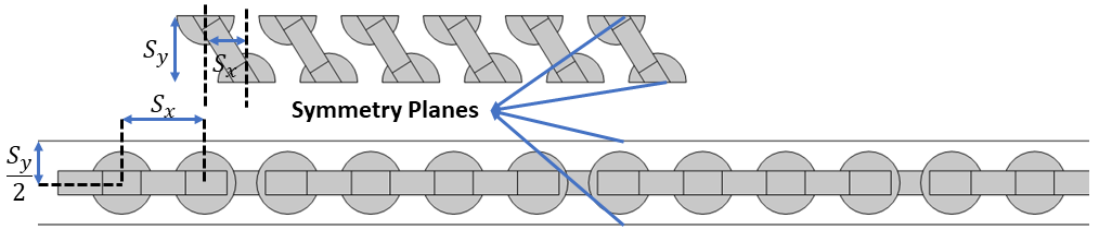

Figure 3.6. Spacings and alignments for both layouts.

The simulations were run for several alignments, spacings, and flow-disturbing structures, and their results are demonstrated in the results section. Inlet air temperature was 25ºC in this simulation. In Figure 3.7, mesh structures and placements of spoilers are shown.

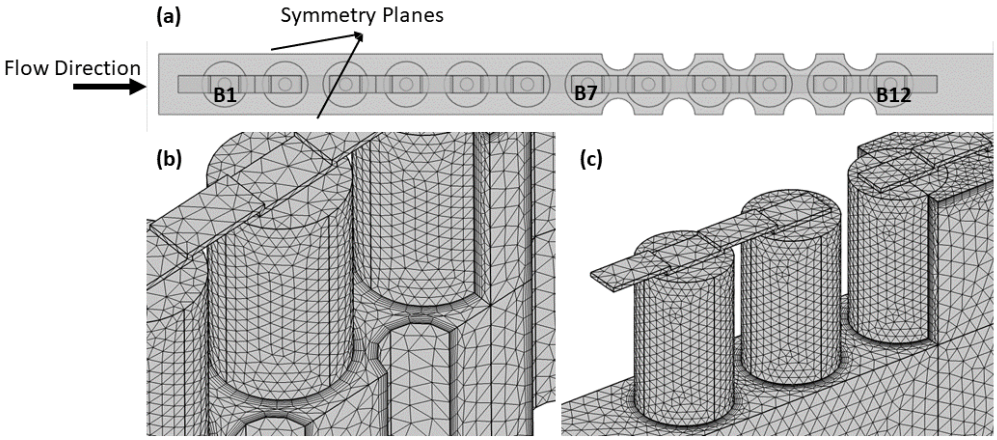

Figure 3.7. (a) top view of simulation with spoilers, (b-c) mesh structures of baffled layout and base design.

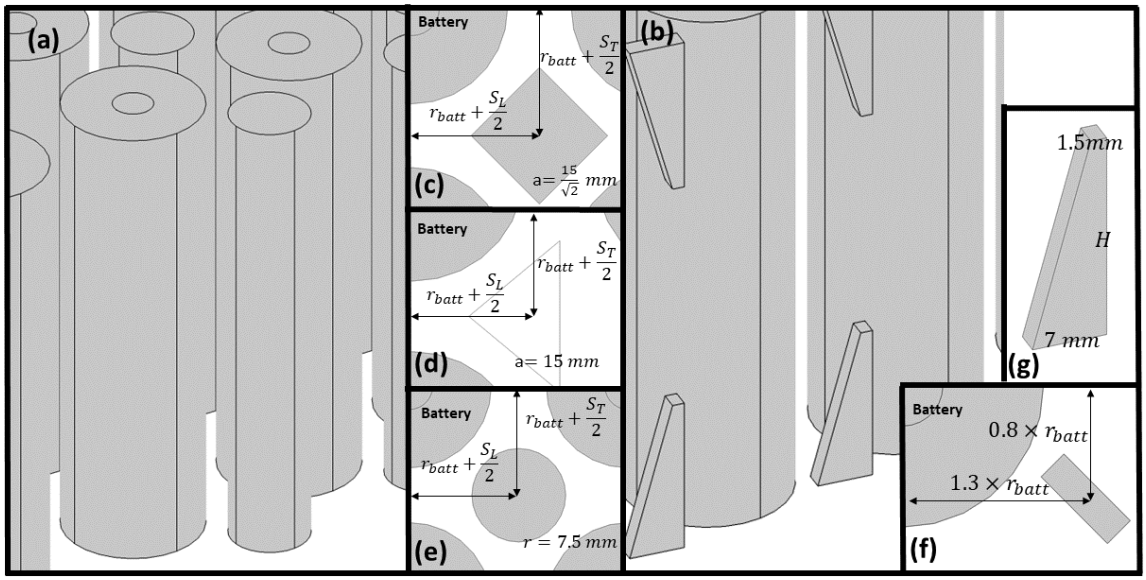

Figure 3.8. The illustration of (a) cylindrical spoilers and (b) winglets in 3D view. Placements of (c) diamond, (d) triangular, (e) cylindrical, and (f) winglet type spoilers from top view. (g) Dimensions of winglet structure.

The centroid of cylindrical, triangular, and diamond shaped spoilers was located equidistantly from adjacent cells. In figure 3.8, spoiler shapes and their placements are

illustrated. All designs illustrated above involve 12 batteries in total, and the inlet velocity of air was 1.65 m/s. Their volumetric power densities were compared to compare their efficiency, which was calculated as in Equation 17, where N_{batt} represents the number of batteries.

$$P_{Vol} = \frac{12 \times 4.2Ah}{S_y \times h_{batt} \times (N_{batt} - 1) \times S_x} \tag{17}$$

CHAPTER 4

RESULTS AND DISCUSSION

Simulation results and validation processes are documented in this section. Besides, the cooling performance of various designs for Lithium-ion battery modules with 12 batteries is documented and compared. The module discharge rate was 3C, and design improvements were made by changing cell-to-cell distances and adding spoilers. To understand the effect of spoilers on thermal efficiency, first, the module simulation was solved for several cell distances without baffles. Then, several cylindrical structures with 6mm diameter were placed between the batteries, especially near those with relatively higher average temperatures. There were several sizes of cylindrical baffles, and the most effective one was the spoiler with a 15mm diameter. Therefore, escribed circle diameters of triangular and diamond-shaped spoilers were set to 15mm as well. Also, winglets were located on the top and bottom walls symmetrically, and their lengths and angles were changed to find the best option. The range for angles was 15°-75°, and winglet lengths were changed between 10mm and 35mm.

4.1. Experimental and Numerical Validation

As expressed in Appendix A, some battery parameters were fitted to the battery. For this reason, a single battery experiment and its simulation were used to validate the battery thermal model. Also, the single battery model was simulated with COMSOL Multiphysics 5.5, and it was subjected to a mesh refinement study. However, since there was no significant dependency on a mesh structure, a mesh structure with 48000 elements was used, as shown in Figure 4.1 (a-b). After setting up the model in COMSOL 5.5, the cell was discharged with 0.1C, 1C, 3C, and 5C. In numerical studies, the battery cell's average surface temperature was compared with the average of three distinct points in experiments at the top, middle, and bottom.

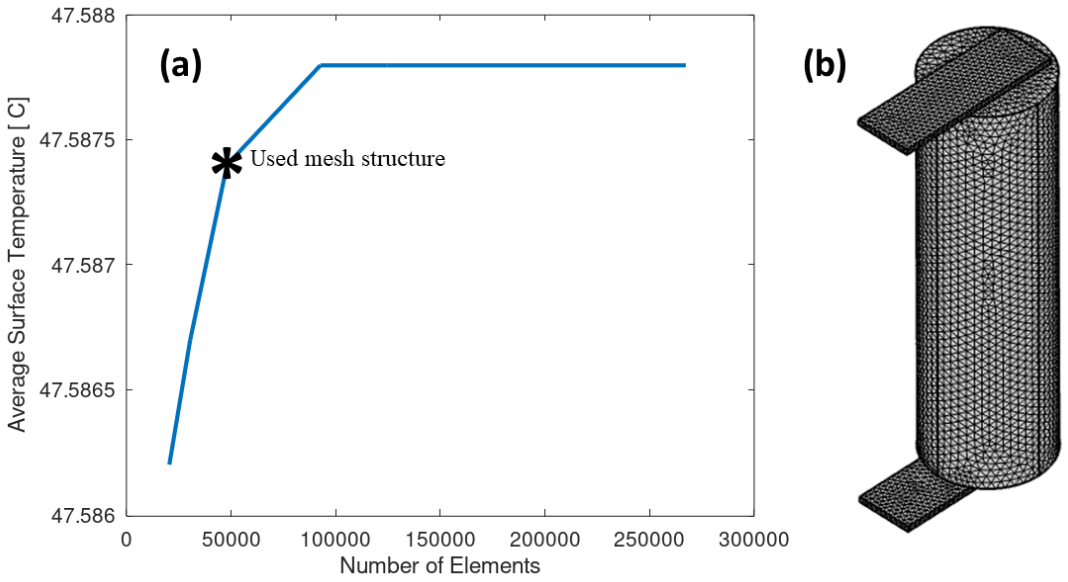

Figure 4.1. (a) mesh dependency curve of surface temperature, (b) mesh structure of the model.

In Figure 4.2, the temperature and voltage curves of different C-rates are given. It can be seen from the figure that the discrepancies between simulation and experiments increase as the discharge rate increases. While the maximum temperature and voltage differences between the simulation and experiment were 3.14ºC and 0.25V for the 3C discharge rate, 5.6ºC and 0.6V were the maximum errors for the 5C. Therefore, the model was used up to 3C.

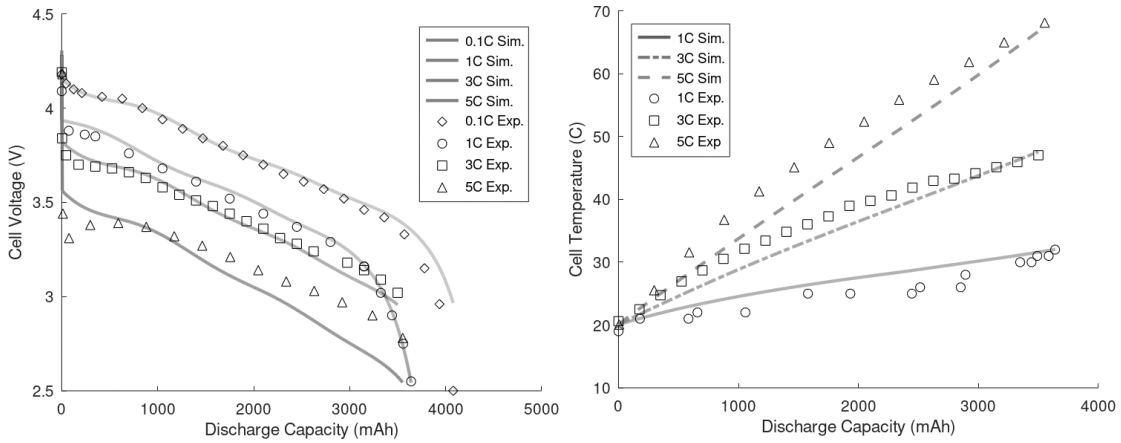

Figure 4.2. The comparison of experimental and simulation temperature and voltage curves.

As for the module simulation, batteries were in a channel of the exact dimensions as the experiment. First, a mesh independency test was conducted by varying the mesh sizes to uncover how many numbers of mesh elements were required for mesh independent simulation results. The errors of various mesh elements are given in Table 4.1. According to the results of grid independence, the mesh with 3.7×10^5 elements was used, as it yields acceptable relative error with the minimum number of mesh elements. The pack was discharged with 3C (25.2 A) for 1120 seconds.

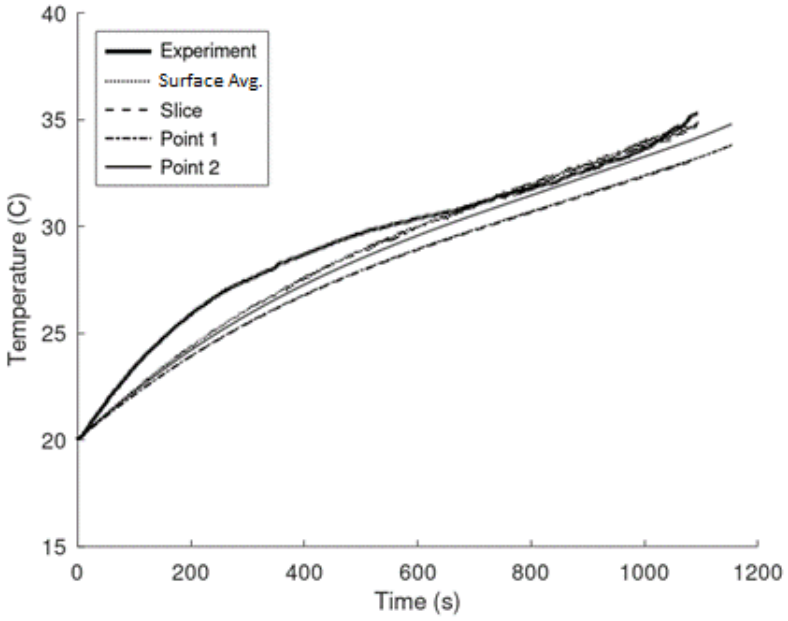

Figure 4.3. Temperature curves of different points on Battery 3.

Temperature and voltage curves of simulations show a similar trend with experiments by few errors, as shown in Figures 4.3, 4.4, and 4.5. In Figure 4.4, the temperature curves of all batteries can be seen, and Figure 4.5 displays voltage curves.

Table 4.1. Velocity measurements of simulation and experiment.

Measuring Point	**Simulation (m/s)**	**Experiment (m/s)**
Inlet	1.629	1.65
Outlet	1.63	1.61
P1 (Fig. 4)	3.55	3.83
P2 (Fig. 4)	3.2	3.58

Table 4.2. Effect of the number of mesh elements on surface temperatures.

Number of Elements	$T_{average,1}$ ℃	$T_{average,2}$ ℃	$T_{average,3}$ ℃	$T_{average,4}$ ℃	$T_{average,5}$ ℃	$T_{average,6}$ ℃
158936	37.685	40.875	41.290	37.717	40.801	41.283
217448	36.881	40.138	40.946	36.906	40.053	40.919
304627	36.754	40.391	41.021	36.794	40.330	40.994
371380	37.193	40.237	40.634	37.175	40.245	40.597
1148084	37.248	40.118	40.516	37.252	40.123	40.492
Number of Elements	$Error_T$ %	$Error_T$ %	$Error_T$ %	$Error_T$ %	$Error_T$ %	$Error_T$ %
158936	-	-	-	-	-	-
217448	2.13	1.80	0.83	2.15	1.83	0.88
304627	0.344	0.63	0.18	0.30	0.69	0.18
371380	1.19	0.38	0.94	1.03	0.21	0.96
1148084	0.148	0.294	0.29	0.20	0.30	0.26

Also, the air velocity was measured at several points in experiments by a hot wire anemometer (Testo 435). Its probe was kept at specific points for 1 minute to measure time-averaged velocities. The velocity comparisons between simulation and experiment are given in Table 4.2.

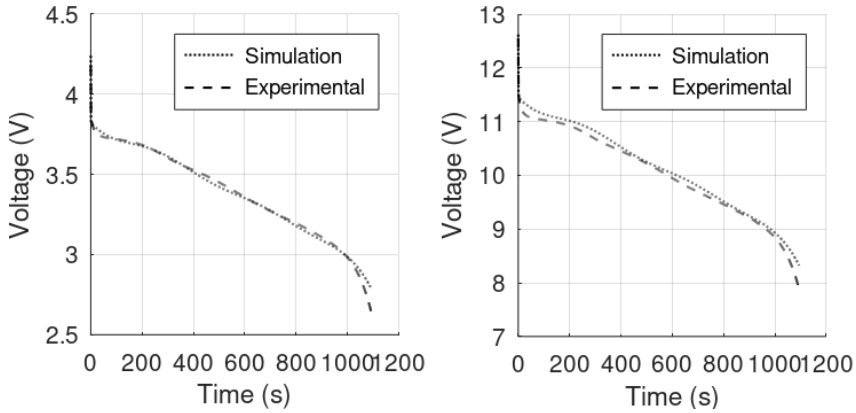

Figure 4.4. Voltage curves of (a) single cell and (b) battery pack.

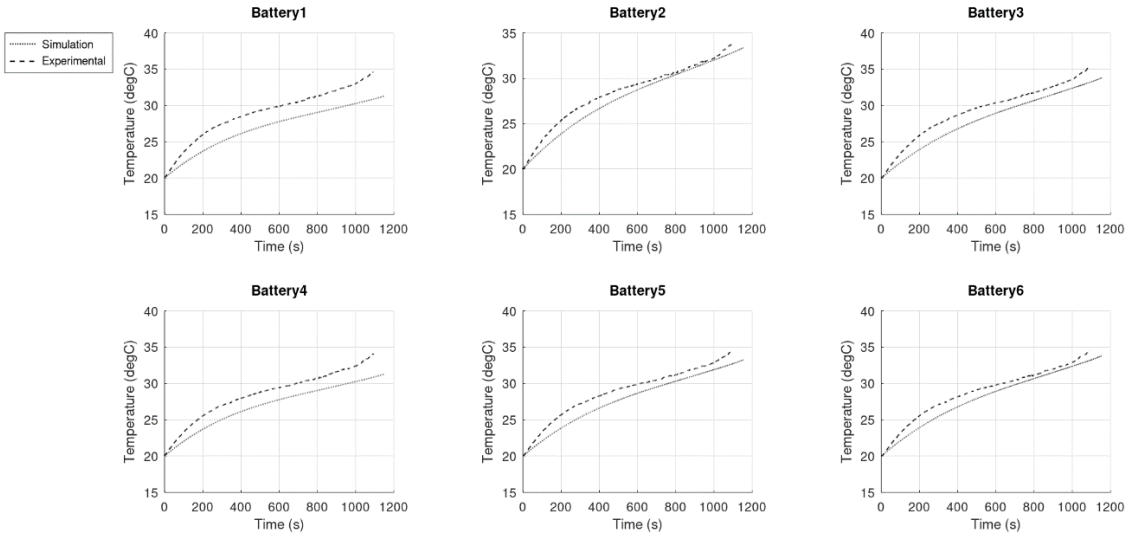

Figure 4.5. Temperature curves of experiments and the same point on simulations for all batteries.

The results show that the battery model and flow simulation are viable for pack simulations. For this reason, the cooling performance of larger battery packs will be investigated and enhanced for the rest of this study. As for the larger modules, another mesh refinement study was conducted for the module with 12 batteries, and it is tabulated in Table 4.3. Since its errors were acceptable, the mesh structure around 7×10^5 elements were used.

Table 4.3. Grid independence results of battery module with 12 cells.

Number of Elements	$T_{average,1}$ ℃	$T_{average,7}$ ℃	$T_{average,12}$ ℃	$T_{average,outlet}$ ℃
632410	34.190	36.206	38.256	32.502
704124	34.182	36.411	38.291	32.442
1021844	34.366	36.283	38.344	32.470
1337197	34.366	36.283	38.344	32.477
Number of Elements	$Error_T$ %	$Error_T$ %	$Error_T$ %	$Error_T$ %
632410	-	-	-	-
704124	0.022	0.567	0.092	0.181
1021844	0.538	0.351	0.138	0.085
1337197	0	0	0	0.021

4.2. The Effect of Battery Spacing

Cell-to-cell distances (δ_{cell}) were investigated for both staggered and inline layouts. As the distance between cells increases, temperature uniformity improves, but it does not affect the maximum temperature significantly, as shown in Figure 4.6. Even though spacious design contains more volume flow rate than congested designs, they cannot provide better cooling because of dead air regions.

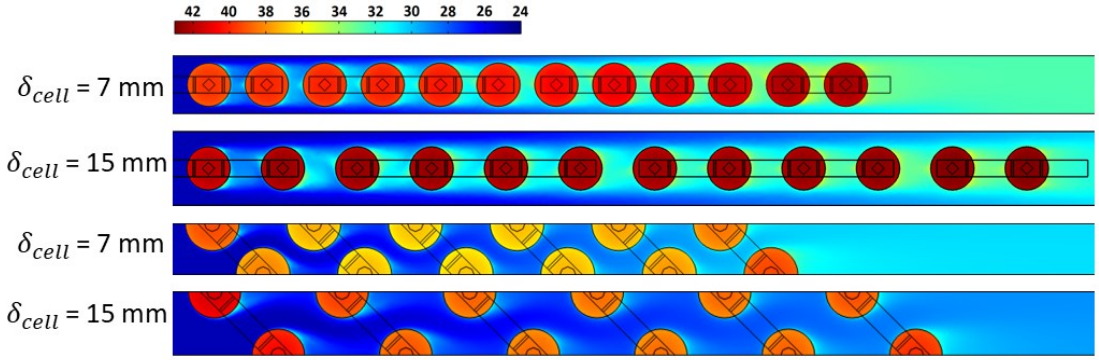

Figure 4.4. Temperature contour (in ºC) of inline and staggered alignments for different spacings.

The temperature contours are generated from the cross-section plane located 35 mm above the battery tabs. It can be interpreted from this section that air cooling mechanisms require improvements that increase the heat transfer coefficient between the battery and air. Many unused cold air regions can be found even in the 7mm designs. Since this cold air leaves the cooling channel without absorbing heat, those designs have the potential for cooling improvement by mixing the coolant.

4.3. The Contribution of Flow Disturbing Structures

In Figure 4.6, for the design with a 7mm cell distance (base design), the average temperature of the air after sixth battery is higher than the entrance. The heat transfer can be increased by changing the flow characteristics after sixth battery. For this purpose, cylindrical blocks were placed between adjacent cells, as shown in Figure 4.7. Since a cylindrical spoiler of 15mm diameter yielded the best results in terms of the temperature

profile, other shapes were fitted inside a 15mm cylinder. Figure 4.7 shows cross-sectional temperature contour of various spoiler designs.

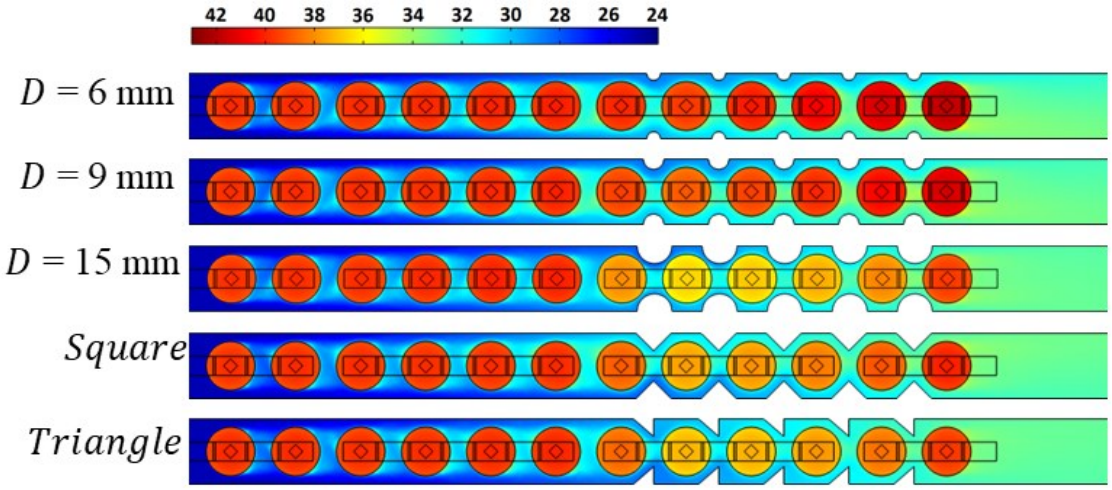

Figure 4.5. Temperature (in ºC) contours of the designs with spoilers.

4.4. The Effectiveness of Winglets

Winglet design optimizations were done based on the angle of attack and winglet height. Since equal sizes of winglets were placed on both walls (top and bottom), its height could not exceed 35 mm (half of cell height). However, 70 mm winglets were placed on only one side for observation purposes. Figure 4.8 shows the angle of attack dependency of fan power consumption (Equation 18), maximum temperature, and temperature gradient. Additionally, fan power consumption was calculated with Equation 18.

$$P_{fan} = U_{in} \times h_{batt} \times S_y \times (P_{in} - P_{out}) \quad (18)$$

The optimum angle was designated as 45º, and the efficiency of different heights was evaluated for this angle. Figures 4.9 and 4.10 show the temperature contours of different angles and heights, respectively.

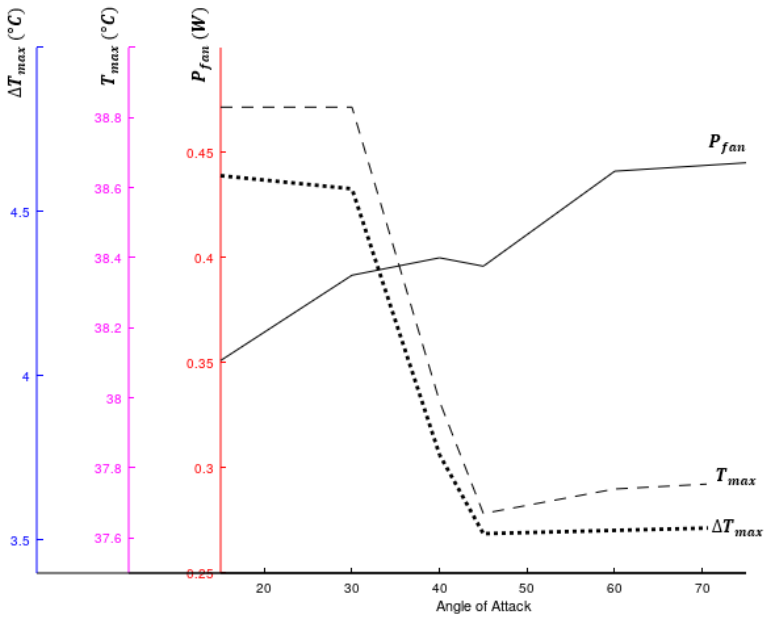

Figure 4.6. Maximum temperature and temperature difference and parasitic power consumption changes over the angle of attack for delta winglet design.

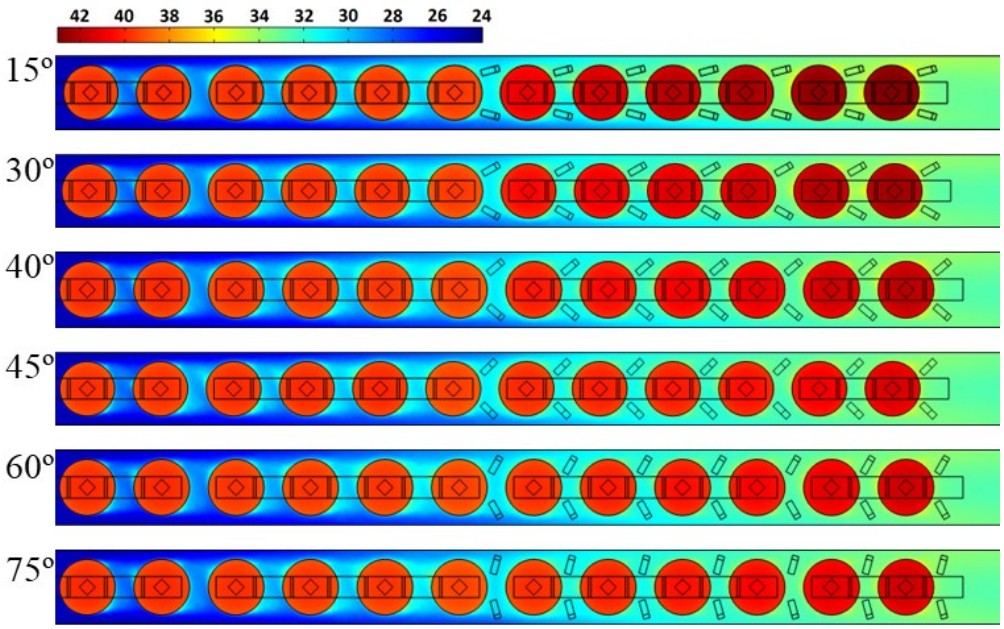

Figure 4.7. Temperature (in ºC) contours of different angles of 20 mm winglets.

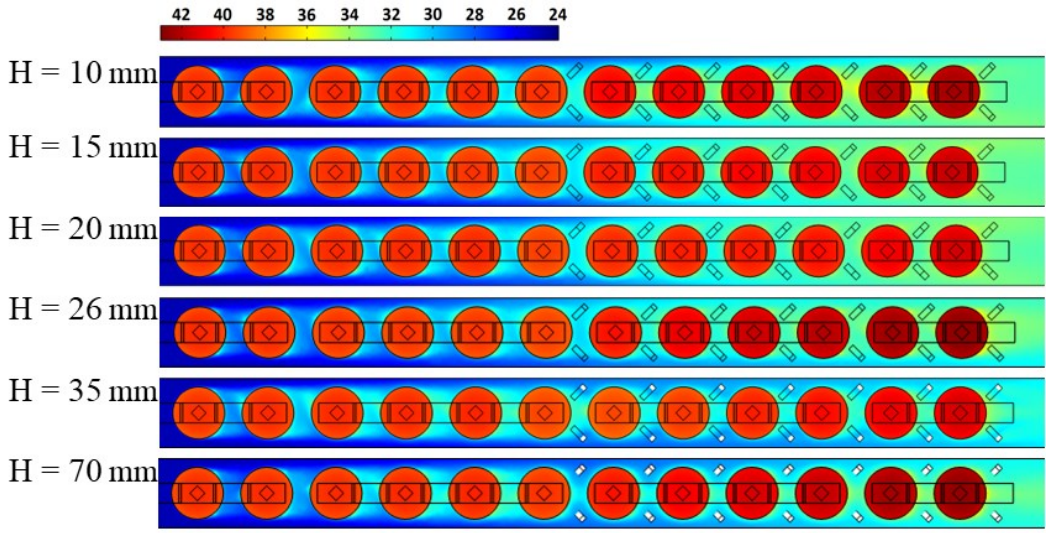

Figure 4.8. Temperature (in ºC) contours of 45º winglets with various heights.

4.5. Comparison of Optimal Designs

In this section, the results of all optimization studies are compared. To keep it short, the designs with reasonable thermal performance are considered. Therefore, winglets with 45º angle of attack; triangular, diamond, and cylindrical spoilers; and base designs ($\delta_{cell} = 7\ mm$) are evaluated. Table 4.4 covers the optimal designs' cooling parameters and fan power consumption. Triangle spoilers yielded the best cooling performance with a significant increase in parasitic power, which is 0.72 W higher than the base design. Also, square and 15 mm cylinders offer a moderate cooling option. In addition, winglet type vortex generators yielded efficient cooling performance with negligible surplus power consumption. Stagger aligned battery packs offer the highest volumetric power density with better cooling performance than the inline alignment, as shown in Figure 4.11 and Table 4.4. It offered 10% better cooling than the best design of the inline alignment. The stagger-aligned pack's volumetric power density was 328 W/l, approximately 17% better than inline alignment. Also, the stagger-aligned design's fan power consumption was relatively low (0.33 W). Figure 4.12 images the surface temperature profiles at the last step of the aforementioned optimal designs.

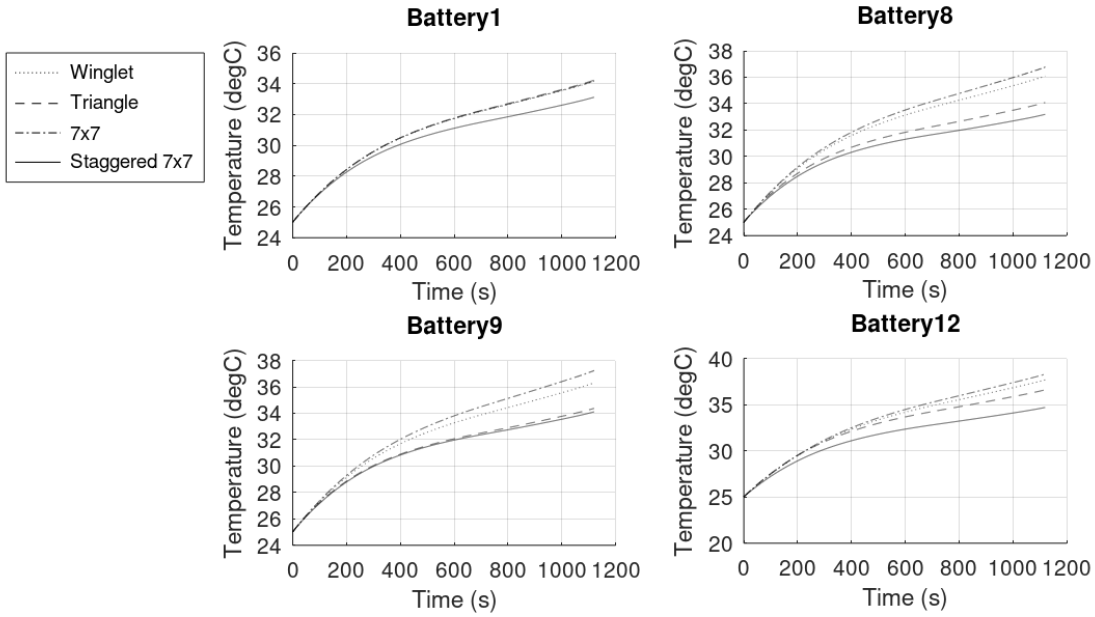

Figure 4.9. Comparison of staggered and baffled designs with the best designs of inline alignment and base design (7×7).

Table 4.4. Outcomes of various designs.

Design	P_{fan} (W)	T_{max} $(°C)$	ΔT_{max} $(°C)$	**Power Density**
$S_x = S_y = 28\ mm$ $\delta_{cell} = 7\ mm$	0.27	38.3	4.12	281 W/l
$S_x = S_y = 36\ mm$ $\delta_{cell} = 15\ mm$	0.095	38.2	2.54	172 W/l
Staggered $\delta_{cell} = 7\ mm$	0.23	35.51	2.7	328 W/l
Cylinder D = 15 mm	0.89	37.14	2.92	281 W/l
Square	0.82	36.91	2.75	
Triangle	0.98	36.6	2.5	
Winglet 10mm 45º	0.33	38.2	3.98	
Winglet 15mm 45º	0.37	37.8	3.6	
Winglet 20mm 45º	0.39	37.7	3.5	
Winglet 26mm 45º	0.45	37.8	3.6	
Winglet 35mm 45º	0.46	38.75	4.53	

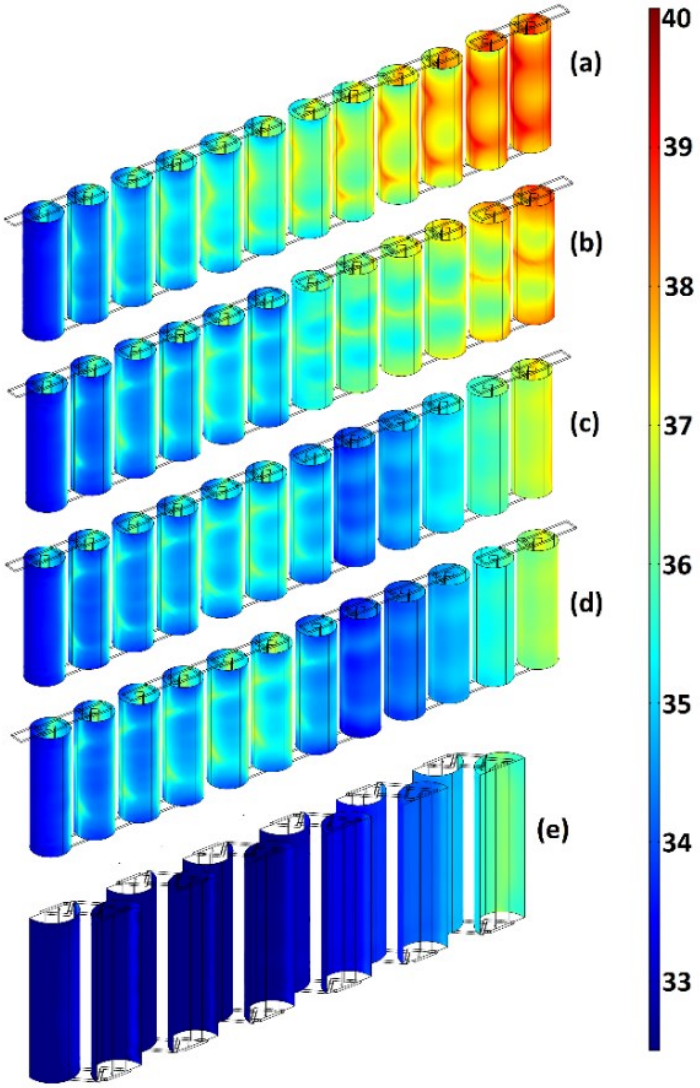

Figure 4.10. Temperature profiles of (a) inline without spoiler, (b) winglet, (c) rectangular, (d) triangular (e) stagger aligned.

It is evident from Figure 4.12 and Table 4.4 that the spoiler structures improve temperature uniformity and reduce the maximum temperature since the heat transfer increases as the baffle structures and winglets create vortices and increase mixing in the hot regions.

4.6. Heat Transfer Performance Parameters

Each design can be clearly compared by adopting a performance parameter used in the heat exchanger literature. Ghobadi et al. [75], used a performance parameter involving the Nusselt number and fanning friction factors, given in Equation 19.

$$\frac{{Nu_b}/{Nu}}{\left({f_b}/{f}\right)^{1/3}} \tag{19}$$

While Nu_b and f_b describe Nusselt number and friction factor of baffled designs, variables without subscripts stand for design without baffles. In this study, the average heat transfer coefficient was put in place of the Nusselt number, and pressure drops were used instead of the friction factor. The performance of all enhancements was compared with the base design (Figure 14 - δ_{cell}=7mm). In Figure 19, the maximum temperature, maximum temperature difference, and heat transfer performance parameters of each design are given. Based on the graph, even though triangular baffles yield the best results, the heat transfer parameter of the triangular design is relatively low due to the high pressure drop of the design. On the other hand, winglet design layouts offer moderate cooling with heat transfer parameters closer to the base design than the triangular layout. Staggered battery alignment provides the best cooling performance with the lowest peak temperature and temperature difference.

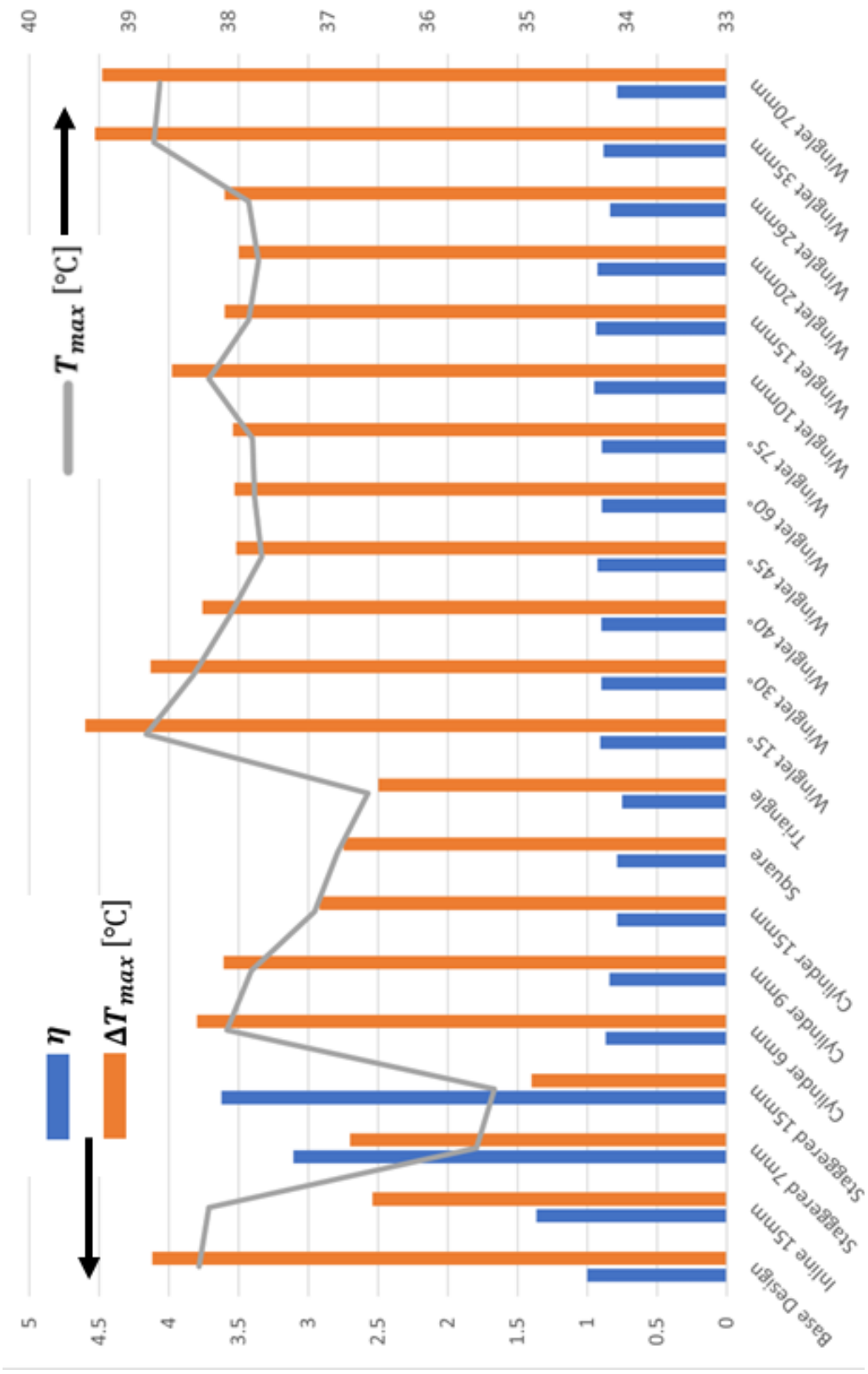

Figure 4.11. Heat transfer performance, maximum temperature differences, and peak temperature comparisons of all designs.

CHAPTER 5

SUMMARY AND CONCLUSION

This thesis highlights the cooling improvement of air-cooled battery modules with additional flow-disturbing structures by conducting numerical studies validated with experiments. The simulation has been done with 3D heat transfer and turbulent flow simulations coupled with a 1D multiscale electrochemical battery model for 21700 cylindrical Lithium-ion cells. Two experiments were performed to confirm the accuracy of the battery model and air-cooling model. Batteries were discharged under a 3C rate while being cooled down by airflow of 1.6 m/s velocity and 25ºC temperature. Spoilers were placed in the module without changing cell-to-cell distances to make comparisons. Mainly four types of spoilers, namely cylindric, triangular, diamond, and winglet vortex generators, were used, and their fan power consumptions, maximum cell temperatures, and temperature gradients were documented. The analyses reached to following results:

(i) As battery distances increase, the temperature gradient improves, but the maximum temperature is not changed. That happens because of stagnant air regions in the cooling channel.

(ii) The cooling performance can be improved by adding spoilers, which mixes the air and increases the heat transfer coefficient between the battery and air. Since spoiler structures can double the fan power consumption, careful optimizations are needed for applications.

(iii) Winglet type vortex generators effectively improve cooling by slightly increasing power consumption. They can be optimum improvement options.

(iv) Staggered layouts are superior to inline arrangements as their positions lead to wavy airflow formation, which increases heat transfer. Also, since the flow path does not change aggressively, pressure drops of staggered systems are moderate.

REFERENCES

[1] M. Wicki, G. Brückmann, F. Quoss, and T. Bernauer, "What do we really know about the acceptance of battery electric vehicles?–Turns out, not much," *Transp. Rev.*, pp. 1–26, 2022, doi: 10.1080/01441647.2021.2023693.

[2] F. Creutzig *et al.*, "Transport: A roadblock to climate change mitigation?," *Science (80-.).*, vol. 350, no. 6263, pp. 911–912, 2015, doi: 10.1126/science.aac8033.

[3] R. Nealer, D. Reichmuth, and D. Anair, "Cleaner Cars from Cradle to Grave: How Electric Cars Beat Gasoline Cars on Lifetime Global Warming Emissions," *Union of Concerned Scientists*. pp. 1–54, 2015, [Online]. Available: https://www.ucsusa.org/sites/default/files/attach/2015/11/Cleaner-Cars-from-Cradle-to-Grave-full-report.pdf%0Ahttp://www.ucsusa.org/sites/default/files/attach/2015/11/Cleaner-Cars-from-Cradle-to-Grave-full-report.pdf.

[4] X. Chen, W. Shen, T. T. Vo, Z. Cao, and A. Kapoor, "An overview of lithium-ion batteries for electric vehicles," in *10th International Power and Energy Conference, IPEC 2012*, 2012, pp. 230–235, doi: 10.1109/ASSCC.2012.6523269.

[5] M. Morris, "Comparison of Rechargeable Battery Technologies," *ASME Early Career Tech. J.*, vol. 11, no. November 2012, pp. 148–155, 2012.

[6] J. Kim, J. Oh, and H. Lee, "Review on battery thermal management system for electric vehicles," *Appl. Therm. Eng.*, vol. 149, no. December, pp. 192–212, 2019, doi: 10.1016/j.applthermaleng.2018.12.020.

[7] S. Ma *et al.*, "Temperature effect and thermal impact in lithium-ion batteries: A review," *Prog. Nat. Sci. Mater. Int.*, vol. 28, no. 6, pp. 653–666, 2018, doi: 10.1016/j.pnsc.2018.11.002.

[8] T. M. Bandhauer, S. Garimella, and T. F. Fuller, "A Critical Review of Thermal Issues in Lithium-Ion Batteries," *J. Electrochem. Soc.*, vol. 158, no. 3, p. R1, 2011, doi: 10.1149/1.3515880.

[9] L. Lu, X. Han, J. Li, J. Hua, and M. Ouyang, “A review on the key issues for lithium-ion battery management in electric vehicles,” *J. Power Sources*, vol. 226, pp. 272–288, 2013, doi: 10.1016/j.jpowsour.2012.10.060.

[10] Y. Fan, Y. Bao, C. Ling, Y. Chu, X. Tan, and S. Yang, “Experimental study on the thermal management performance of air cooling for high energy density cylindrical lithium-ion batteries,” *Appl. Therm. Eng.*, vol. 155, no. February, pp. 96–109, 2019, doi: 10.1016/j.applthermaleng.2019.03.157.

[11] A. Pesaran, “Battery Thermal Management in EVs and HEVs : Issues and Solutions,” *Adv. Automot. Batter. Conf.*, no. January 2001, p. 10, 2001.

[12] A. K. Thakur *et al.*, “A state of art review and future viewpoint on advance cooling techniques for Lithium–ion battery system of electric vehicles,” *J. Energy Storage*, vol. 32, no. April, p. 101771, 2020, doi: 10.1016/j.est.2020.101771.

[13] J. Kim, J. Oh, and H. Lee, “Review on battery thermal management system for electric vehicles,” *Appl. Therm. Eng.*, vol. 149, no. November 2018, pp. 192–212, 2019, doi: 10.1016/j.applthermaleng.2018.12.020.

[14] J. Chen *et al.*, “Effects of different phase change material thermal management strategies on the cooling performance of the power lithium ion batteries: A review,” *J. Power Sources*, vol. 442, no. October, p. 227228, 2019, doi: 10.1016/j.jpowsour.2019.227228.

[15] J. Jaguemont, N. Omar, P. Van den Bossche, and J. Mierlo, “Phase-change materials (PCM) for automotive applications: A review,” *Appl. Therm. Eng.*, vol. 132, pp. 308–320, 2018, doi: 10.1016/j.applthermaleng.2017.12.097.

[16] D. Chen, J. Jiang, G. H. Kim, C. Yang, and A. Pesaran, “Comparison of different cooling methods for lithium ion battery cells,” *Appl. Therm. Eng.*, vol. 94, pp. 846–854, 2016, doi: 10.1016/j.applthermaleng.2015.10.015.

[17] J. Xie, Z. Ge, M. Zang, and S. Wang, “Structural optimization of lithium-ion battery pack with forced air cooling system,” *Appl. Therm. Eng.*, vol. 126, pp. 583–593, 2017, doi: 10.1016/j.applthermaleng.2017.07.143.

[18] N. Yang, X. Zhang, G. Li, and D. Hua, “Assessment of the forced air-cooling performance for cylindrical lithium-ion battery packs: A comparative analysis between aligned and staggered cell arrangements,” *Appl. Therm. Eng.*, vol. 80, pp. 55–65, 2015, doi: 10.1016/j.applthermaleng.2015.01.049.

[19] S. Gocmen and E. Cetkin, “Emergence of elevated battery positioning in air cooled battery packs for temperature uniformity in ultra-fast dis/charging applications,” *J. Energy Storage*, vol. 45, no. June 2021, p. 103516, 2021, doi: 10.1016/j.est.2021.103516.

[20] R. Mahamud and C. Park, “Reciprocating air flow for Li-ion battery thermal management to improve temperature uniformity,” *J. Power Sources*, vol. 196, no. 13, pp. 5685–5696, 2011, doi: 10.1016/j.jpowsour.2011.02.076.

[21] T. Wang, K. J. Tseng, and J. Zhao, “Development of efficient air-cooling strategies for lithium-ion battery module based on empirical heat source model,” *Appl. Therm. Eng.*, vol. 90, pp. 521–529, 2015, doi: 10.1016/j.applthermaleng.2015.07.033.

[22] E. Jiaqiang *et al.*, “Effects of the different air cooling strategies on cooling performance of a lithium-ion battery module with baffle,” *Appl. Therm. Eng.*, vol. 144, no. August, pp. 231–241, 2018, doi: 10.1016/j.applthermaleng.2018.08.064.

[23] S. Shahid and M. Agelin-Chaab, “Development and analysis of a technique to improve air-cooling and temperature uniformity in a battery pack for cylindrical batteries,” *Therm. Sci. Eng. Prog.*, vol. 5, no. November 2017, pp. 351–363, 2018, doi: 10.1016/j.tsep.2018.01.003.

[24] T. F. Fuller, M. Doyle, and J. Newman, “Simulation and Optimization of the Dual Lithium Ion Insertion Cell,” *J. Electrochem. Soc.*, vol. 141, no. 1, pp. 1–10, 1994, doi: 10.1149/1.2054684.

[25] D. K. Sharma and A. Prabhakar, “A review on air cooled and air centric hybrid thermal management techniques for Li-ion battery packs in electric vehicles,” *J. Energy Storage*, vol. 41, no. May, p. 102885, 2021, doi: 10.1016/j.est.2021.102885.

[26] N. Nitta, F. Wu, J. T. Lee, and G. Yushin, “Li-ion battery materials: Present and future,” *Mater. Today*, vol. 18, no. 5, pp. 252–264, 2015, doi: 10.1016/j.mattod.2014.10.040.

[27] M. Bianchini, M. Roca-Ayats, P. Hartmann, T. Brezesinski, and J. Janek, “There and Back Again—The Journey of LiNiO2 as a Cathode Active Material,” *Angew. Chemie - Int. Ed.*, vol. 58, no. 31, pp. 10434–10458, 2019, doi: 10.1002/anie.201812472.

[28] H. Y. Tran, C. Täubert, and M. Wohlfahrt-Mehrens, “Influence of the technical process parameters on structural, mechanical and electrochemical properties of LiNi0.8Co0.15Al0.05O2 based electrodes - A review,” *Prog. Solid State Chem.*, vol. 42, no. 4, pp. 118–127, 2014, doi: 10.1016/j.progsolidstchem.2014.04.006.

[29] A. R. M. Siddique, S. Mahmud, and B. Van Heyst, “A comprehensive review on a passive (phase change materials) and an active (thermoelectric cooler) battery thermal management system and their limitations,” *J. Power Sources*, vol. 401, no. September, pp. 224–237, 2018, doi: 10.1016/j.jpowsour.2018.08.094.

[30] S. Wu, L. Lao, L. Wu, L. Liu, C. Lin, and Q. Zhang, “Effect analysis on integration efficiency and safety performance of a battery thermal management system based on direct contact liquid cooling,” *Appl. Therm. Eng.*, vol. 201, no. PA, p. 117788, 2022, doi: 10.1016/j.applthermaleng.2021.117788.

[31] M. Petzl and M. A. Danzer, “Nondestructive detection, characterization, and quantification of lithium plating in commercial lithium-ion batteries,” *J. Power Sources*, vol. 254, pp. 80–87, 2014, doi: 10.1016/j.jpowsour.2013.12.060.

[32] H. Liu, Z. Wei, W. He, and J. Zhao, “Thermal issues about Li-ion batteries and recent progress in battery thermal management systems: A review,” *Energy Convers. Manag.*, vol. 150, no. August, pp. 304–330, 2017, doi: 10.1016/j.enconman.2017.08.016.

[33] S. Santhanagopalan, Q. Zhang, K. Kumaresan, and R. E. White, “Parameter Estimation and Life Modeling of Lithium-Ion Cells,” *J. Electrochem. Soc.*, vol. 155, no. 4, p. A345, 2008, doi: 10.1149/1.2839630.

[34] Y. Fan, Y. Bao, C. Ling, Y. Chu, X. Tan, and S. Yang, “Experimental study on the thermal management performance of air cooling for high energy density cylindrical lithium-ion batteries,” *Appl. Therm. Eng.*, vol. 155, no. December 2018, pp. 96–109, 2019, doi: 10.1016/j.applthermaleng.2019.03.157.

[35] D. Lisbona and T. Snee, “A review of hazards associated with primary lithium and lithium-ion batteries,” *Process Saf. Environ. Prot.*, vol. 89, no. 6, pp. 434–442, 2011, doi: 10.1016/j.psep.2011.06.022.

[36] N. Williard, W. He, C. Hendricks, and M. Pecht, “Lessons learned from the 787 dreamliner issue on Lithium-Ion Battery reliability,” *Energies*, vol. 6, no. 9, pp. 4682–4695, 2013, doi: 10.3390/en6094682.

[37] Q. Wang, P. Ping, X. Zhao, G. Chu, J. Sun, and C. Chen, “Thermal runaway caused fire and explosion of lithium ion battery,” *J. Power Sources*, vol. 208, pp. 210–224, 2012, doi: 10.1016/j.jpowsour.2012.02.038.

[38] Y. Liu and J. Zhang, “Design a J-type air-based battery thermal management system through surrogate-based optimization,” *Appl. Energy*, vol. 252, no. May, p. 113426, 2019, doi: 10.1016/j.apenergy.2019.113426.

[39] H. Hirano, T. Tajima, T. Hasegawa, T. Sekiguchi, and M. Uchino, “Boiling liquid battery cooling for electric vehicle,” *IEEE Transp. Electrif. Conf. Expo, ITEC Asia-Pacific 2014 - Conf. Proc.*, pp. 1–4, 2014, doi: 10.1109/ITEC-AP.2014.6940931.

[40] R. W. Van Gils, D. Danilov, P. H. L. Notten, M. F. M. Speetjens, and H. Nijmeijer, “Battery thermal management by boiling heat-transfer,” *Energy Convers. Manag.*, vol. 79, pp. 9–17, 2014, doi: 10.1016/j.enconman.2013.12.006.

[41] C. Roe *et al.*, “Immersion cooling for lithium-ion batteries – A review,” *J. Power Sources*, vol. 525, no. August 2021, p. 231094, 2022, doi: 10.1016/j.jpowsour.2022.231094.

[42] S. Al Hallaj and J. R. Selman, “A Novel Thermal Management System for Electric Vehicle Batteries Using Phase-Change Material,” *J. Electrochem. Soc.*, vol. 147,

no. 9, p. 3231, 2000, doi: 10.1149/1.1393888.

[43] C. Lin, S. Xu, G. Chang, and J. Liu, “Experiment and simulation of a LiFePO4 battery pack with a passive thermal management system using composite phase change material and graphite sheets,” *J. Power Sources*, vol. 275, pp. 742–749, 2015, doi: 10.1016/j.jpowsour.2014.11.068.

[44] Z. Wang, H. Zhang, and X. Xia, “Experimental investigation on the thermal behavior of cylindrical battery with composite paraffin and fin structure,” *Int. J. Heat Mass Transf.*, vol. 109, pp. 958–970, 2017, doi: 10.1016/j.ijheatmasstransfer.2017.02.057.

[45] P. R. Tete, M. M. Gupta, and S. S. Joshi, “Developments in battery thermal management systems for electric vehicles: A technical review,” *J. Energy Storage*, vol. 35, no. September 2020, p. 102255, 2021, doi: 10.1016/j.est.2021.102255.

[46] Z. Y. Jiang and Z. G. Qu, “Lithium–ion battery thermal management using heat pipe and phase change material during discharge–charge cycle: A comprehensive numerical study,” *Appl. Energy*, vol. 242, no. February, pp. 378–392, 2019, doi: 10.1016/j.apenergy.2019.03.043.

[47] J. Liang, Y. Gan, and Y. Li, “Investigation on the thermal performance of a battery thermal management system using heat pipe under different ambient temperatures,” *Energy Convers. Manag.*, vol. 155, no. October 2017, pp. 1–9, 2018, doi: 10.1016/j.enconman.2017.10.063.

[48] J. Zhao, P. Lv, and Z. Rao, “Experimental study on the thermal management performance of phase change material coupled with heat pipe for cylindrical power battery pack,” *Exp. Therm. Fluid Sci.*, vol. 82, pp. 182–188, 2017, doi: 10.1016/j.expthermflusci.2016.11.017.

[49] T. Han, B. Khalighi, E. C. Yen, and S. Kaushik, “Li-ion battery pack thermal management: Liquid versus air cooling,” *J. Therm. Sci. Eng. Appl.*, vol. 11, no. 2, 2019, doi: 10.1115/1.4041595.

[50] R. Sabbah, R. Kizilel, J. R. Selman, and S. Al-Hallaj, “Active (air-cooled) vs.

passive (phase change material) thermal management of high power lithium-ion packs: Limitation of temperature rise and uniformity of temperature distribution," *J. Power Sources*, vol. 182, no. 2, pp. 630–638, 2008, doi: 10.1016/j.jpowsour.2008.03.082.

[51] L. H. Saw, Y. Ye, A. A. O. Tay, W. T. Chong, S. H. Kuan, and M. C. Yew, "Computational fluid dynamic and thermal analysis of Lithium-ion battery pack with air cooling," *Appl. Energy*, vol. 177, pp. 783–792, 2016, doi: 10.1016/j.apenergy.2016.05.122.

[52] X. Yu, Z. Lu, L. Zhang, L. Wei, X. Cui, and L. Jin, "Experimental study on transient thermal characteristics of stagger-arranged lithium-ion battery pack with air cooling strategy," *Int. J. Heat Mass Transf.*, vol. 143, p. 118576, 2019, doi: 10.1016/j.ijheatmasstransfer.2019.118576.

[53] X. Na, H. Kang, T. Wang, and Y. Wang, "Reverse layered air flow for Li-ion battery thermal management," *Appl. Therm. Eng.*, vol. 143, no. July, pp. 257–262, 2018, doi: 10.1016/j.applthermaleng.2018.07.080.

[54] G. Zhao, X. Wang, M. Negnevitsky, and H. Zhang, "A review of air-cooling battery thermal management systems for electric and hybrid electric vehicles," *J. Power Sources*, vol. 501, no. May, p. 230001, 2021, doi: 10.1016/j.jpowsour.2021.230001.

[55] R. D. Jilte, R. Kumar, and L. Ma, "Thermal performance of a novel confined flow Li-ion battery module," *Appl. Therm. Eng.*, vol. 146, no. February 2018, pp. 1–11, 2019, doi: 10.1016/j.applthermaleng.2018.09.099.

[56] H. Zhou, F. Zhou, L. Xu, J. Kong, and QingxinYang, "Thermal performance of cylindrical Lithium-ion battery thermal management system based on air distribution pipe," *Int. J. Heat Mass Transf.*, vol. 131, pp. 984–998, 2019, doi: 10.1016/j.ijheatmasstransfer.2018.11.116.

[57] N. Yang, X. Zhang, G. Li, and D. Hua, "Assessment of the forced air-cooling performance for cylindrical lithium-ion battery packs: A comparative analysis between aligned and staggered cell arrangements," *Appl. Therm. Eng.*, vol. 80, pp.

55–65, 2015, doi: 10.1016/j.applthermaleng.2015.01.049.

[58] A. Bejan and S. Lorente, “Design with Constructal Theory,” *Design with Constructal Theory*. pp. 1–529, 2008, doi: 10.1002/9780470432709.

[59] Z. Lu, X. Z. Meng, L. C. Wei, W. Y. Hu, L. Y. Zhang, and L. W. Jin, “Thermal management of densely-packed EV battery with forced air cooling strategies,” *Energy Procedia*, vol. 88, pp. 682–688, 2016, doi: 10.1016/j.egypro.2016.06.098.

[60] T. Yang, N. Yang, X. Zhang, and G. Li, “Investigation of the thermal performance of axial-flow air cooling for the lithium-ion battery pack,” *Int. J. Therm. Sci.*, vol. 108, pp. 132–144, 2016, doi: 10.1016/j.ijthermalsci.2016.05.009.

[61] P. Dubey, G. Pulugundla, and A. K. Srouji, “Direct Comparison of Immersion and Cold-Plate Based Cooling for Automotive Li-Ion Battery Modules,” *Energies*, vol. 14, no. 5, p. 1259, 2021, doi: 10.3390/en14051259.

[62] G. Xia, L. Cao, and G. Bi, “A review on battery thermal management in electric vehicle application,” *J. Power Sources*, vol. 367, pp. 90–105, 2017, doi: 10.1016/j.jpowsour.2017.09.046.

[63] M. Suresh Patil, J. H. Seo, and M. Y. Lee, “A novel dielectric fluid immersion cooling technology for Li-ion battery thermal management,” *Energy Convers. Manag.*, vol. 229, no. December 2020, p. 113715, 2021, doi: 10.1016/j.enconman.2020.113715.

[64] C. Zhao, W. Cao, T. Dong, and F. Jiang, “Thermal behavior study of discharging/charging cylindrical lithium-ion battery module cooled by channeled liquid flow,” *Int. J. Heat Mass Transf.*, vol. 120, pp. 751–762, 2018, doi: 10.1016/j.ijheatmasstransfer.2017.12.083.

[65] M. S. Patil, J. H. Seo, S. Panchal, S. W. Jee, and M. Y. Lee, “Investigation on thermal performance of water-cooled Li-ion pouch cell and pack at high discharge rate with U-turn type microchannel cold plate,” *Int. J. Heat Mass Transf.*, vol. 155, p. 119728, 2020, doi: 10.1016/j.ijheatmasstransfer.2020.119728.

[66] D. W. Sundin and S. Sponholtz, “Thermal management of Li-ion batteries with single-phase liquid immersion cooling,” *IEEE Open J. Veh. Technol.*, vol. 1, no. December 2019, pp. 82–92, 2020, doi: 10.1109/OJVT.2020.2972541.

[67] S. Panchal, I. Dincer, M. Agelin-Chaab, R. Fraser, and M. Fowler, “Experimental and theoretical investigations of heat generation rates for a water cooled LiFePO4 battery,” *Int. J. Heat Mass Transf.*, vol. 101, pp. 1093–1102, 2016, doi: 10.1016/j.ijheatmasstransfer.2016.05.126.

[68] T. Amalesh and N. Lakshmi Narasimhan, “Liquid cooling vs hybrid cooling for fast charging lithium-ion batteries: A comparative numerical study,” *Appl. Therm. Eng.*, vol. 208, no. September 2021, p. 118226, 2022, doi: 10.1016/j.applthermaleng.2022.118226.

[69] P. Qin, M. Liao, D. Zhang, Y. Liu, J. Sun, and Q. Wang, “Experimental and numerical study on a novel hybrid battery thermal management system integrated forced-air convection and phase change material,” *Energy Convers. Manag.*, vol. 195, no. May, pp. 1371–1381, 2019, doi: 10.1016/j.enconman.2019.05.084.

[70] W. Wu, X. Yang, G. Zhang, K. Chen, and S. Wang, “Experimental investigation on the thermal performance of heat pipe-assisted phase change material based battery thermal management system,” *Energy Convers. Manag.*, vol. 138, pp. 486–492, 2017, doi: 10.1016/j.enconman.2017.02.022.

[71] MOLICEL®, “PRODUCT DATA SHEET MODEL INR-21700-P42A,” Maple Ridge, Canada, 2015. [Online]. Available: https://www.imrbatteries.com/content/molicel_p42a.pdf.

[72] “The k-ε Turbulence Model,” *COMSOL Multiphysics® v. 5.5*. https://doc.comsol.com/5.5/doc/com.comsol.help.cfd/cfd_ug_fluidflow_single.06.088.html.

[73] COMSOL Multiphysics®, “COMSOL Multiphysics® v. 5.5.” COMSOL AB, Stockholm, Sweden, [Online]. Available: www.comsol.com.

[74] H. Chen *et al.*, “A Simplified Mathematical Model for Heating-Induced Thermal

Runaway of Lithium-Ion Batteries," *J. Electrochem. Soc.*, vol. 168, no. 1, p. 010502, 2021, doi: 10.1149/1945-7111/abd64c.

[75] B. Ghobadi, F. Kowsary, and F. Veysi, "Optimization of heat transfer and pressure drop of the channel flow with baffle," *High Temp. Mater. Process.*, vol. 40, no. 1, pp. 286–299, 2021, doi: 10.1515/htmp-2021-0030.

[76] S. Basu *et al.*, "Non-isothermal electrochemical model for lithium-ion cells with composite cathodes," *J. Power Sources*, vol. 283, pp. 132–150, 2015, doi: 10.1016/j.jpowsour.2015.02.127.

[77] N. A. Chaturvedi, R. Klein, J. Christensen, J. Ahmed, and A. Kojic, "Modeling, estimation, and control challenges for lithium-ion batteries," *Proc. 2010 Am. Control Conf. ACC 2010*, no. June 2010, pp. 1997–2002, 2010, doi: 10.1109/acc.2010.5531623.

[78] M. Safari and C. Delacourt, "Modeling of a Commercial Graphite/LiFePO4 Cell," *J. Electrochem. Soc.*, vol. 158, no. 5, p. A562, 2011, doi: 10.1149/1.3567007.

[79] K. J. Lee, K. Smith, A. Pesaran, and G. H. Kim, "Three dimensional thermal-, electrical-, and electrochemical-coupled model for cylindrical wound large format lithium-ion batteries," *J. Power Sources*, vol. 241, pp. 20–32, 2013, doi: 10.1016/j.jpowsour.2013.03.007.

[80] V. Srinivasan and C. Y. Wang, "Analysis of Electrochemical and Thermal Behavior of Li-Ion Cells," *J. Electrochem. Soc.*, vol. 150, no. 1, pp. A98–A106, 2003, doi: 10.1149/1.1526512.

APPENDIX A

GOVERNING EQUATIONS FOR BATTERY MODEL

In the multiscale battery model, lithium ions are transferred in 1D, the path between two electrodes, since there is a significant length scale difference between other directions [76]. However, the phase change of ions between the solid and liquid states is defined in the 2D spherical domain, and ion transfer occurs in a porous media.

$$\frac{\partial c_s}{\partial t} = \frac{D_s}{r^2}\frac{\partial}{\partial r}\left(r^2 \frac{\partial c_s}{\partial r}\right) \tag{A.1}$$

Equation A.1 defines the solid-state mass transfer in porous electrodes. The boundary conditions are given in Equations A.2 and A.3.

$$\left.\frac{\partial c_s}{\partial r}\right|_{r=0} = 0 \tag{A.2}$$

$$\left.\frac{\partial c_s}{\partial r}\right|_{r=r_p} = \frac{j^{Li+}}{a_s F} \tag{A.3}$$

Where a_s stands for effective surface area, which is:

$$a_s = \frac{3\varepsilon_s}{r_p} \tag{A.4}$$

The phase change occurs on the surface of spherical particles as much as the current density $\left(j^{Li+}\right)$. Liquid-state ion transfer is defined by Equation A.5 with the boundary conditions Equations A.6-A.11.

$$\frac{\partial \varepsilon_l c_l}{\partial t} = \frac{\partial}{\partial x}\left(D_l^{eff}\frac{\partial c_l}{\partial x}\right) + \frac{1 - t_+^0}{F} j^{Li+} \tag{A.5}$$

Equations A.6 and A.7 are called no-flux boundary conditions since current collectors do not contain ions, and Equations A.8-A.11 define electrode-separator interfaces [77].

$$\left.\frac{\partial c_l}{\partial x}\right|_{x=0} = 0 \tag{A.6}$$

$$\left.\frac{\partial c_l}{\partial x}\right|_{x=L_{batt}} = 0 \tag{A.7}$$

$$\varepsilon_l \left(\frac{\partial c_l}{\partial x}\right)\Big|_{x=L_{neg}} = \varepsilon_{l,sep}\left(\frac{\partial c_l}{\partial x}\right)\Big|_{x=L_{neg}} \tag{A.8}$$

$$\varepsilon_l \left(\frac{\partial c_l}{\partial x}\right)\Big|_{x=L_{neg}+L_{sep}} = \varepsilon_{l,sep} \left(\frac{\partial c_l}{\partial x}\right)\Big|_{x=L_{neg}+L_{sep}} \quad \text{(A.9)}$$

$$c_l\left(L_{neg}, t\right) = c_{l,sep}\left(L_{neg}, t\right) \quad \text{(A.10)}$$

$$c_{l,sep}\left(L_{neg} + L_{sep}, t\right) = c_l\left(L_{neg} + L_{sep}, t\right) \quad \text{(A.11)}$$

Also, there are charge balance equations identifying the balance between the number of Lithium ions transferred and the amount of charge transfer, coupled with mass transfer equations and electrochemical kinetics equations. The potential in the solid phase is defined with Ohm's law, which is given in Equation A.12 with its boundary conditions Equations A.13- A.16.

$$\frac{\partial}{\partial x}\left(\sigma_s^{eff} \frac{\partial \Phi_s}{\partial x}\right) = j^{Li+} \quad \text{(A.12)}$$

$$\sigma_s^{eff} \frac{\partial \Phi_s}{\partial x}\Big|_{x=L_{batt}} = -I_{app} \quad \text{(A.13)}$$

$$\sigma_s^{eff} \frac{\partial \Phi_s}{\partial x}\Big|_{x=L_{neg}+L_{sep}} = 0 \quad \text{(A.14)}$$

$$\sigma_s^{eff} \frac{\partial \Phi_s}{\partial x}\Big|_{x=L_{neg}} = 0 \quad \text{(A.15)}$$

$$\Phi_s|_{x=0} = 0 \quad \text{(A.16)}$$

The charge balance in the liquid phase is expressed with Equation A.17, and its boundary conditions are defined in Equations A.18-A.21:

$$\frac{\partial}{\partial x}\left(\kappa^{eff} \frac{\partial \Phi_l}{\partial x}\right) + \frac{\partial}{\partial x}\left(\frac{2RT\kappa^{eff}}{F}(t_+^0 - 1)\left(1 + \frac{d \ln f_{\pm}}{d \ln c_l}\right)\frac{\partial \ln c_l}{\partial x}\right) = -j^{Li+} \quad \text{(A.17)}$$

$$\frac{\partial \Phi_l}{\partial x}\Big|_{x=0} = 0 \quad \text{(A.18)}$$

$$\frac{\partial \Phi_s}{\partial x}\Big|_{x=L_{batt}} = 0 \quad \text{(A.19)}$$

$$\Phi_l\left(L_{neg}, t\right) = \Phi_l\left(L_{neg}, t\right) \quad \text{(A.20)}$$

$$\Phi_l\left(L_{neg} + L_{sep}, t\right) = \Phi_l\left(L_{neg} + L_{sep}, t\right) \quad \text{(A.21)}$$

Ultimately, the relation between the total current and potentials is described by the Butler-Volmer equation, which is given in Equation A.22.

$$j^{Li+} = a_s i_0 \left[exp\left(\frac{\alpha_a F}{RT}\eta\right) - exp\left(-\frac{\alpha_c F}{RT}\eta\right)\right] \quad \text{(A.22)}$$

The equivalent voltage for the cathode is a polynomial, whose parameters were fitted with the polynomial regression method based on the 0.1C discharge curve and anode equivalent voltage curve from the literature [78]. Cathode voltage polynomial coefficients are given in Table A.1, and equivalent voltage functions are given in Equations A.23 and A.24.

$$E_{eq,pos} = \sum_{i=0}^{22} A_i x^i \quad \text{(A.23)}$$

$$E_{eq,neg} = 0.6379 + 0.5416exp(-305.5309 \times y) + 0.044\ \tanh\left(-\frac{y-0.1958}{0.1088}\right) - 0.1978\ \tanh\left(\frac{y-1.0571}{0.0854}\right) - 0.6875\tanh\left(\frac{y+0.0117}{0.0529}\right) - 0.0175\tanh\left(\frac{y-0.5692}{0.0875}\right) \quad \text{(A.24)}$$

Table A.1. Polynomial coefficients for cathode equivalent voltage.

Coef.	Value	Coef.	Value	Coef.	Value
A_0	*398.01336013198392*	A_8	*496823.58244024246*	A_{16}	*31493.18267972166*
A_1	*-6296.1076950394308*	A_9	*-421106.34179412422*	A_{17}	*-1084234.1893559622*
A_2	*41959.219071580315*	A_{10}	*354200.00761110592*	A_{18}	*92159.424582747262*
A_3	*-147857.02171270244*	A_{11}	*-490432.27097464772*	A_{19}	*819007.96409683058*
A_4	*287870.02690709516*	A_{12}	*356826.47806278308*	A_{20}	*197218.48943382909*
A_5	*-295327.71817991912*	A_{13}	*-295625.16819127946*	A_{21}	*-778437.66013222793*
A_6	*180105.05120692172*	A_{14}	*138640.00521595744*	A_{22}	*285035.16062089079*
A_7	*-271903.1222659052*	A_{15}	*509484.82719697087*		

Material properties of the cell are given in Table A.3. Equations A.25-A.27 define the solid-state diffusion coefficient of the cathode, liquid state diffusion, and liquid state electronic conductivity, respectively [76].

$$D_{s,pos} = \frac{3.3 \times 10^{-13}}{(x-0.02)^2} \quad \text{(A.25)}$$

$$D_l = 10^{-\left(4.43+\left(\frac{54}{\left(T-\left(229+5\left(\frac{c_l}{1000}\right)\right)\right)}\right)+0.22\frac{c_l}{1000}\right)} \times 10^{-4} \quad \text{(A.26)}$$

$$\sigma_l = \left(-8.2488 + 0.053248T - 2.9871 \times 10^{(-5T^2)} + 0.26235\left(\frac{c_l}{1000}\right) - 9.3063 \times 10^{\left(-3\frac{c_l}{1000}T\right)} + 8.069 \times 10^{\left(-6\frac{c_l}{1000}T^2\right)} + 0.22002\left(\frac{c_l}{1000}\right)^2 - 1.765 \times 10^{\left(-4\left(\frac{c_l}{1000}\right)^2 T\right)}\right)^2 \left(\frac{c_l}{10000}\right) \quad \text{(A.27)}$$

The active layer thicknesses and reaction rates (i_0) were changed based on the experimental data by adjusting them for battery capacity and overpotential heat generation. The fitted reaction rates for each discharge rate are given in Table A.2.

Table A.2. Reaction rates for anode and cathode.

C-rate	Anode	Cathode
0.1	0.5	3
1	0.015	0.07
3	0.0063	0.013
5	0.0008	0.0008

Table A.3. Battery parameters.

**Fitted parameters based on the single battery experiment.*

Parameter	**Anode**	**Separator**	**Cathode**	**CC-**	**CC+**	**Ref.**
Length (μm)	17	16	13	15	10	*
ε_l	0.3825	0.47	0.3382	-	-	[76]
ε_s	0.5802	-	0.4483	-	-	[76]
α_a & α_c	0.5	-	0.5	-	-	[76]
c_s^{max} (mol/m^3)	28200	-	49195	-	-	[76]
c_s^0 (mol/m^3)	$0.65 \times c_s^{max}$	-	$0.41 \times c_s^{max}$	-	-	[79]
σ_s & σ_l (S/m)	16700	cf. Eq. (A.27)	0.04	-	-	[76]
D_s & D_l (m^2/s)	1×10^{-3}	cf. Eq. (A.26)	cf. Eq. (A.25)	-	-	[76]
$\rho\ (kg/m^3)$	2500	1200	3000	-	-	[76]
$C_p\ (J/kg/K)$	800	800	1000	385	875	[76], [80]
$k\ (W/m/K)$	1.04	1	2	398	200	[76], [80]
c_l^0	1150	1150	1150	-	-	*
c_l^{ref}	1000	-	1000	-	-	*